THE EFFECT OF TIDAL FORCING ON IRON CYCLING IN INTERTIDAL SALT MARSH SEDIMENTS

A Thesis
Presented to
The Academic Faculty

by

Gwendolyn M. Bristow

In Partial Fulfillment
of the Requirements for the Degree
Master of Science in the
School of Earth & Atmospheric Sciences, Georgia Institute of Technology

Georgia Institute of Technology
August, 2006

THE EFFECT OF TIDAL FORCING ON IRON CYCLING IN INTERTIDAL SALT MARSH SEDIMENTS

Approved by:

Dr. Martial Taillefert, Advisor
School of Earth and Atmospheric Sciences
Georgia Institute of Technology

Dr. Ellery Ingall
School of Earth and Atmospheric Sciences
Georgia Institute of Technology

Dr. Emanuele Di Lorenzo
School of Earth and Atmospheric Sciences
Georgia Institute of Technology

Date Approved: July 10, 2006

ACKNOWLEDGEMENTS

I would like to thank the following people for their help with this project: David Bull, Elizabeth Carey, Stephanie Chow, Dr. Ellery Ingall, Stephanie Neuhuber, Jennifer Newton, Don Nuzzio of Analytical Instrument Systems, Inc., Dian Putrasahan, Dr. Carolyn Ruppel, Skidaway Institute of Oceanography, Dr. Martial Taillefert, Farhana Yasmin, and my Thesis Advisory Committee.

TABLE OF CONTENTS

LIST OF TABLES

Page

LIST OF FIGURES

Page

SUMMARY

In this study we investigated the effect of tidal forcing on iron cycling in intertidal saltmarsh sediments (ISS). Historically, sulfate has been considered the major terminal electron acceptor involved in organic carbon remineralization in ISS. Although sulfate is a more efficient electron acceptor for organic matter degradation in anoxic ISS, iron's rapid recycling at the surface of ISS may allow it also to be an important electron acceptor for the remineralization of organic matter. Bioturbation, macrophyte-mediated irrigation, and semidiurnal tidal forcing in this environment may increase the abundance of O_2 in the top few cm of the sediment, rapidly oxidizing iron and inhibiting sulfate reduction. To determine if the cycling of iron may be faster than previously thought in these sediments, we combined sediment core chemical profiles of reduced and oxidized insoluble iron with in-situ electrochemical profiles of O_2, Fe^{2+}, soluble organic-Fe^{3+} complexes, $FeS_{(aq)}$, and ΣH_2S in the top few centimeters of unvegetated creek bank sediments over several tidal cycles. We also installed monitoring wells in the tidal creek bank to quantify tidal forcing and to investigate tidal direction in the sediments. We built a transient, reactive transport model to simulate measured geochemical profiles and test our understanding of diagenetic processes. Additional tests were run on the model to investigate the importance of bioirrigation compared to tidally-induced porewater advection. Results indicate that tidal action is a more dominant transport process. It affects the cycling of iron in ISS by flushing reduced species out of the sediment during flood tide, and allowing oxygen and oxidized species deeper into the sediment during ebb tide. As a result, amorphous iron oxides are replenished at the sediment surface, and microbial

iron reduction may be the main respiratory process in the first tens of centimeters of creek bank saltmarsh sediments subjected to intense tidal forcing.

CHAPTER 1

INTRODUCTION

The global carbon budget must be understood and quantified in order to predict future atmospheric CO_2 concentrations and their effects on the oceans. Recently, continental margins have been adopted as a new reservoir in carbon budget analysis (Liu et al., 2000). According to recent reports, biogeochemical processes and active cross-shelf transport in continental margins may be pronounced enough to influence the carbon cycle of the ocean as a whole (Liu et al. 2000). Some models predict that three quarters of marine carbon burial may take place in the continental margins (Liu et al. 2000). Global carbon budgets estimate that a large proportion of terrestrial organic matter is remineralized or converted to marine organic matter on continental margins (Hedges, et al. 1997) before it enters the deeper ocean. These discrepancies call for a more thorough investigation of diagenetic processes in continental margins.

Saltmarshes are continental margin regions with high primary productivity (Alongi, 1998) and receive substantial terrestrial input of organic matter. Subsequently there is a large supply of highly bioavailable organic matter to the sediment. Some of the highest measured rates of microbial organic carbon oxidation occur in saltmarshes (Alongi 1998). Oxygen is the first terminal electron acceptor consumed in the breakdown of this fresh organic matter. Then in anoxic sediments, organic carbon can undergo bacterially-mediated oxidation using terminal electron acceptors according to their thermodynamic sequence as in Table 1 (Froelich 1979).

Table 1. Heterotrophic, autotrophic, and abiotic reactions, adapted from Froelich et al., 1979.

Heterotrophic Reactions	ΔG^{0*} - [kJ/mol]
$(CH_2O)_x(NH_3)_y(H_3PO_4) + xO_2 + yH^+ \rightarrow xCO_2 + yNH_4^+ + H_3PO_4 + xH_2O$	-3190
$(CH_2O)_x(NH_3)_y(H_3PO_4) + 2xMnO_2 + (4x+y)H^+ \rightarrow xCO_2 + 2xMn^{2+} + yNH_4^+ + H_3PO_4 + 3xH_2O$	-3090
$(CH_2O)_x(NH_3)_y(H_3PO_4) + \frac{4}{5}xNO_3^- + \left(\frac{4}{5}x+y\right)H^+ \rightarrow xCO_2 + \frac{2}{5}xN_2 + yNH_4^+ + H_3PO_4 + \frac{7}{5}xH_2O$	-3030
$(CH_2O)_x(NH_3)_y(H_3PO_4) + \frac{x}{2}NO_3^- + (x+y)H^+ \rightarrow xCO_2 + \frac{x}{2}NH_4^+ + yNH_4^+ + H_3PO_4 + \frac{x}{2}H_2O$	-2750
$(CH_2O)_x(NH_3)_y(H_3PO_4) + 4xFeOOH + (8x+y)H^+ \rightarrow xCO_2 + 4xFe^{2+} + yNH_4^+ + H_3PO_4 + 7xH_2O$	-1330
$(CH_2O)_x(NH_3)_y(H_3PO_4) + \frac{x}{2}SO_4^{2-} + (x+y)H^+ \rightarrow xCO_2 + \frac{x}{2}H_2S + yNH_4^+ + H_3PO_4 + xH_2O$	-380
$(CH_2O)_x(NH_3)_y(H_3PO_4) + yH^+ \rightarrow \frac{x}{2}CO_2 + \frac{x}{2}CH_4 + yNH_4^+ + H_3PO_4$	-350

* assuming Redfield ratio for $(CH_2O)_x(NH_3)_y(H_3PO_4)$, x = 106 and y = 16 (Froelich et al., 1979)

Side Chemical and/or Autotrophic Reactions
$4Fe^{2+} + O_2 + 10H_2O \rightarrow 4Fe(OH)_{3(s)} + 8H^+$ *
$4Mn^{2+} + O_2 + 2H_2O \rightarrow 2MnO_{2(s)} + 4H^+$
$NH_4^+ + 2O_2 \rightarrow NO_3^- + H_2O + 2H^+$
$2H_2S + O_2 \rightarrow 2S^{(0)} + 2H_2O$
$CH_4 + 2O_2 \rightarrow CO_2 + 2H_2O$
$Mn^{2+} + Solid \rightarrow Mn_{ads}$ *
$Fe^{2+} + Solid \rightarrow Fe_{ads}$ *
$MnO_2 + H_2S + 2H^+ \rightarrow Mn^{2+} + S^{(0)} + 2H_2O$ *
$MnO_2 + Fe^{2+} + 4H_2O \rightarrow Mn^{2+} + 2Fe(OH)_{3(s)} + 2H^+$ *
$2Fe(OH)_{3(s)} + H_2S + 4H^+ \rightarrow 2Fe^{2+} + S^{(0)} + 6H_2O$ *
$Mn^{2+} + HCO_3^- \rightarrow MnCO_{3(s)} + H^+$ *
$Fe^{2+} + HCO_3^- \rightarrow FeCO_{3(s)} + H^+$ *
$Fe^{2+} + H_2S \rightarrow FeS_{(s)} + 2H^+$ *
$FeS_{(s)} + H_2S \rightarrow FeS_{2(s)} + H_{2(g)}$ *

* = chemical reactions mainly

1

End-products of anaerobic organic matter oxidation are small organic molecules, CO_2, DIC and the reduced species: N_2, NH_4^+, Mn^{2+}, Fe^{2+}, ΣH_2S (H_2S, HS^-, and S^{2-}), and CH_4. In salt marshes, nitrate reduction occurs rapidly and depletes the generally low nitrate concentrations in the top centimeters of the sediment (Gribsholt et al. 2003). Mn-oxides are easily dissolved and reduced, and are chemically stable in the reduced form (Stumm and Morgan 1996). Therefore, Mn-oxides are not considered a major terminal electron acceptor for organic carbon remineralization. Ferric iron, however, may be an important terminal electron acceptor in these environments. Microbial iron reduction generally receives little attention in salt marsh sediments because ferric iron is a weaker terminal electron acceptor than sulfate: just one mole of carbon is oxidized for every four moles of iron reduced (Table 1). Historically, the primary reductant of ferric iron in marine sediments is considered to be sulfide generated from sulfate-reducing bacterial (SRB) activity (Koretsky et al. 2003, Millero 1991). Ferric iron may also be reduced by dissolved organic-Fe(II) complexes (Zinder et al. 1986) or by organics themselves (Zinder et al. 1986, Lakind and Stone 1989, Luther et al. 1992, Bonnidetti et al. 1993, Doong and Schink 2002).

SRB are obligate anaerobes (Berner 1980) which utilize the large supply of available sulfate in marine sediments with great efficiency-- each molecule of sulfate can oxidize two moles of carbon (See Table 1). SRB may outcompete methanogenic bacteria for energy supply (Abrams and Nedwell 1978). Therefore, when ample sulfide is present, methanogenesis is not considered a substantial means of carbon oxidation. As a result, sulfate reduction is historically considered the primary pathway for carbon remineralization here (Hines et al. 1989, Alongi 1998), and this process generates great

amounts of sulfide in salt marsh sediments. However, recent evidence suggests that ferric iron may be reduced during microbially-mediated organic carbon oxidation (Canfeld et al. 1993, Lowe et al. 2000), and this may be an important process if local physical forcing reoxidizes iron with enough frequency.

In many cases, the importance of a particular terminal electron accepting process for organic carbon oxidation depends on the mechanisms by which the reduced end product can be reoxidized. In the case of iron, these processes are crucial to determining its importance as a terminal electron acceptor. Abiotic oxidation of ferrous iron and sulfide is known to occur. Fe^{2+} rapidly oxidizes to ferric oxyhydroxides or amorphous Fe-oxides (i.e., $Fe(OH)_3$) in the presence of O_2 (Stumm and Morgan 1996) (Table 1). Fe^{2+} oxidation in the presence of organic ligands may form highly soluble organic-Fe(III) complexes (Taillefert et al. 2000). However, the types of organic species capable of complexation with iron in marine sediments are unknown, as is their degree of heterogeneity. Sulfide is abiotically oxidized by O_2 in salt marshes, but the reaction is relatively slow (Millero 1989).

Terminal electron acceptors may also be replenished through microbial oxidation pathways. Recent research has investigated the role of iron-oxidizing bacteria (FeOB) (Kappler and Newman 2003). Microbial nitrification exists near the sediment-water interface (SWI), but is inhibited by HS^- (Joye et al. 1995). Rapid aerobic microbial Mn(II) oxidation may occur, but the mechanism is not well understood (Bargar et al. 2000). Microbially-mediated aerobic methane oxidation is well known to occur. Recent evidence suggests that anaerobic oxidation of methane may happen in the presence of

SRB (Boetius et al. 2000); This process may produce H_2, which SRB use to reduce sulfate (Valentine and Reeburgh 2000).

Other important abiotic chemical processes that can prevent recycling of reduced metabolites are at work in the salt marsh. Deep in the sediment, iron is commonly sequestered in the precipitates $FeS_{(s)}$ and $FeS_{2(s)}$ that are formed from ΣH_2S and reduced iron species. $FeS_{(aq)}$ is an intermediate formed by the reaction of Fe^{2+} and ΣH_2S (Theberge and Luther 1997), and is a cluster of unknown stoichiometry that seems to be a precursor to $FeS_{(s)}$ precipitation. It is easily detected by voltammetric microelectrodes, although uncertainty about the $FeS_{(aq)}$ makeup means its concentration cannot yet be quantified through this method. $FeS_{(aq)}$ may also react with $H_2S_{(aq)}$ to form pyrite (FeS_2). (Rickard and Luther 1997, Rickard 1997) (Table 1). $FeS_{(s)}$ precipitates are quite stable in anoxic conditions but may be oxidized by O_2, Mn-oxides (Yao and Millero 1993) and Fe-oxides (Canfield 1992).

In addition to biological and chemical reactions, diagenesis in salt marshes is further complicated by physical processes. Bioturbation due to fiddler crabs *Uca pugnax* (Gribsholt and Kostka 2003), and irrigation due to abundant local growth of the sea grass *Spartina alterniflora* (Howes 1981) introduce oxygen deeper into the sediment (Sundby et al. 1998), allowing for rapid oxidation of reduced iron deeper than the SWI. Bioturbation is historically considered the major physical forcing in salt marsh sediments (Furukawa et al. 2001), and consequently has received the most attention from geochemists.

Interestingly, most of the literature on the role of hydrology in coastal environments covers the influence of surface water hydrological regimes on the ecology

and geomorphology of salt marshes (Bolster and Saiers 2002, Mann and Wetzel 2000, Mwamba and Torres 2002), the role of tides on sandy sediments biogeochemistry (Huettel et al. 1998, Reimers et al. 2004), and the role of freshwater and seawater intrusions on water resources (Hughes et al. 1998, Schultz and Ruppel 2002). In turn, the role of tidal forcing on biogeochemical processes involved in the cycling of natural organic matter is largely ignored. However, strong advection induced by tidal flow may alter sediment geochemistry by causing movement of reduced species to oxic sediments or oxidized species to reduced sediments. This is important because if oxidation due to tidal advection can replenish considerable ferric iron, the effect of microbial iron reduction on carbon remineralization in salt marsh sediments may be more significant than previously thought.

Because physical, biological, and chemical processes are intertwined in an intertidal salt marsh, high resolution analytical techniques are needed to investigate the role of iron in the cycling of carbon there. Standard methods for geochemical redox species characterization in sediments do not allow the frequency of sampling required for analysis of intertidal sediments. Conventional oceanographic methods involve taking sediment cores processed ex-situ, and utilizing pH and other ion-specific electrodes (ISEs), such as O_2 and sulfide (Reimers et al. 1986, Glud et al. 1994, Canfeld et al. 1993). However, ex-situ core processing is too time-intensive, and ISEs are not able to measure various redox species at the same location at the same time for direct comparison.

In-situ voltammetry, used in this study, enables multiple redox species to be measured simultaneously using just a single electrode. Furthermore, sampling time for a voltammetric scan is on the order of seconds, a resolution that facilitates investigation of

rapid processes occurring in salt marsh sediments. Unfortunately, the consequences of such ease and high frequency of analyses are large quantities of electrochemical data. While too much data may be considered a luxury problem, it necessitated the development of a computer program to decrease data analysis processing time. In this paper, we introduce the program Voltint, a Matlab program built for expeditious voltammetric data integration.

In this study we combine conventional geochemical measurements, in-situ electrochemical analyses, and porewater advection measurements with a mathematical model to test our hypothesis that tidally-induced advection plays a role in iron cycling in intertidal salt marsh sediments. Electrochemical data presented in this paper represent some of the first in situ measurements with high temporal resolution obtained in an intertidal salt marsh environment.

Results indicate that tidally induced porewater advection may drive iron cycling in intertidal creek bank sediments. In this situation, reduced iron may be periodically transported to an oxic environment, where it is oxidized and made available as a terminal electron acceptor in the remineralization of organic matter. In this way, iron cycling may play a meaningful role in the carbon cycle.

CHAPTER 2

METHODS

Sampling area

The study location is the Saltmarsh Ecosystem Research Facility (SERF), an intertidal salt marsh influenced by a semidiurnal tide located at Skidaway Institute of Oceanography in Savannah, GA (Figure 1).

Tidal creek

Figure 1. Sampling location: an intertidal salt marsh creek at the Skidaway Institute of Oceanography (SKIO) near Savannah, GA.

Sampling took place in a tidal creek bank of the lower marsh, where there was significant fiddler crab bioturbation. Abundant *Spartina alterniflora,* a tall sea grass, grew adjacent to the creek bank, however the sample site itself was unvegetated. In this creek bank, parts of the sediment may be exposed to the atmosphere during low tide,

while at high tide the sediment is under approximately 2 m of water. Salinity in the area taken during three summers ranged between 19 (June, 2003) and 30 ppt (July, 2004). Water temperatures ranged from 39.7 to 40.1 ˚C. Sediment temperature (July, 2004) was 29.5 ˚C.

Sampling events

7.5 cm diameter short cores were taken in the creek bank in the summer of 2002 using polycarbonate corers. They were processed for chemical depth profiles of dissolved ferric and ferrous iron and amorphous and crystalline iron oxide. In June of 2003, in-situ electrochemical measurements were taken at this location for 14 hours, with four electrodes placed at depths 0, 3.5, 7, and 10.5 cm into the sediment. In July of 2004, similar in-situ electrochemical measurements were made in the same location over a period of 45 hours with electrodes at 0, 7, and 11 cm deep in the sediment.

Geochemistry

Short cores were processed in a glove bag within one hour of sampling, under a nitrogen atmosphere, to keep samples anoxic. Cores were sliced into approximately 5 mm thick sections and centrifuged in a glove bag to extract porewaters. Porewaters were filtered with 0.2 micron polyethersulfone Whatman filters, then processed for dissolved Fe^{2+} and Fe_{Total} using the ferrozine method of Stookey (1970). Dissolved Fe^{3+} was determined as the difference between Fe_{Total} and Fe^{2+}. The sediment was stored in parafilmed 50 ml falcon tubes and then frozen for solid ferric iron analysis at a later time. Amorphous iron oxides were determined using the ascorbate extraction method of Kostka and Luther (1994), and total solid iron (Crystalline Fe-oxides and AVS) using the dithionite extraction method of Kostka and Luther (1994).

Electrochemistry

In-situ electrochemical time series profiles were carried out in the creek bank sediment using voltammetry. Fe^{2+}, soluble organic Fe(III) (Taillefert et al. 2000), ΣH_2S, O_2, Mn^{2+}, and $FeS_{(aq)}$ (Theberge and Luther 1997) can be measured by this method. In voltammetry, a potential is applied between two electrodes (called the working and reference electrodes), and currents are produced when redox species at the working electrode tip are oxidized or reduced. The current issued by each redox reaction is measured as a function of the potential, and redox species are identified by the potential at which they generate current. These induced currents are detected at a third electrode, called the counter electrode. The reference electrode, which acts as the anode, was a standard Ag/AgCl electrode. The counter electrode was a platinum wire. The working electrode, which acts as a cathode, was a Au/Hg amalgam on a 100 micron gold wire. In situ voltammetry data were generated with an underwater DLH-60d (Analytical Systems, Inc.). This instrument contains a potentiostat and datalogger in a waterproof housing. It may be programmed in advance and left in the saltmarsh to automatically run voltammetric scans at defined time intervals. It also enables the user to run up to four working voltammetric electrodes sequentially. In this configuration, the four working electrodes were placed at differing but fixed depths with a computer-controlled micromanipulator attached to an aluminum lander (built in-house, Figure 2). The reference and counter electrodes were attached directly to the lander. The submersible potentiostat was positioned on the lander, which was then lowered into the sediment. Data files were processed using Voltint, a home-made Matlab® program that presents the voltammograms in a graphical user interface (GUI). Currents and standard deviations of

the currents for all the species at differing times and electrodes were converted to concentrations by the Pilot Ion Method of Brendel and Luther (1995), with Mn^{2+} as the pilot ion. Organic-Fe(III) and $FeS_{(aq)}$ data are reported in currents, for their exact chemical compositions are unknown and calibrations are not available.

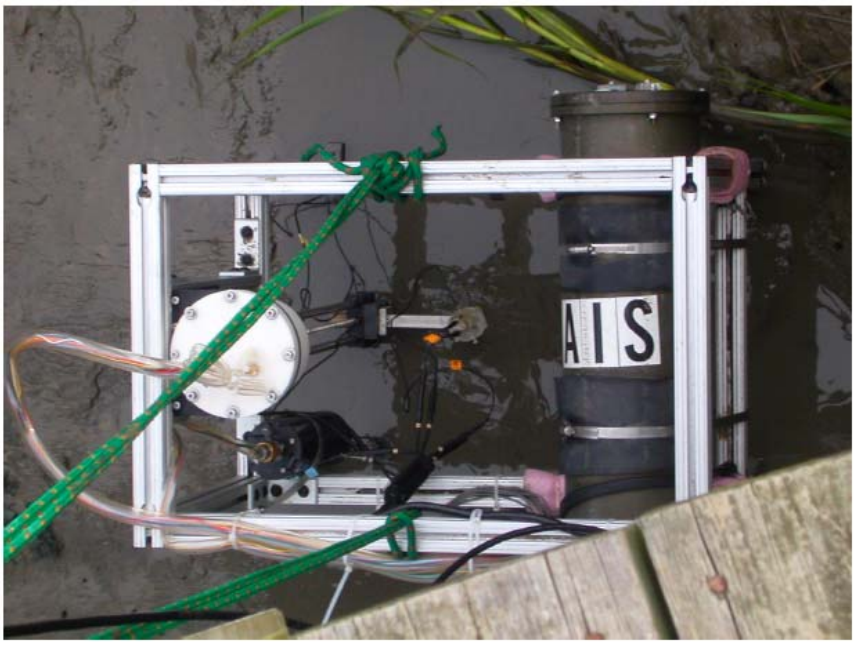

Figure 2. Lander deployment for voltammetric in-situ time series measurements. On the right: submersible potentiostat (DLH-60d Analytical Systems Inc.). On the left, electrodes and micromanipulator.

Voltammetric data interpretation and processing

In voltammetric experiments, a range of potentials is applied to electrodes in solution, and current response is measured. Voltammetric methods exploit the fact that specific redox reactions are instigated by certain applied electrical potentials. Because redox reactions involve a transfer of electrons, they can be observed by measuring electron flow at the electrode surface where the redox reaction takes place.

Typically, current measurements taken in voltammetry are represented as the current as a function of applied potential, known as a voltammogram. In order to identify and quantify the detected species, the currents generated from the redox reaction must be extracted from the voltammogram.

Multiple currents are generated when a potential is applied to an electrode over time. Aside from the current produced by chemical species as they undergo reactions, known as the Faradaic current, a capacitance current is generated each time a pulse of potential is applied between the electrode and the solution. During the scan, the electrode becomes negatively charged. The negative charge attracts positive ions from solution nearby. These two types of charges form layers which act as plates of a capacitor to generate a current. This capacitance current is background noise that needs to be minimized using modulation of the potential applied to the working electrode. Two types of modulations are generally employed for these investigations:

Linear sweep voltammetry (LSV) is used for the detection of dissolved oxygen in natural waters and as a test for electrode quality. In LSV, a linearly increasing direct current (DC) potential is applied to the electrode as a function of time. Cyclic voltammetry applies a linear DC potential as well, but returns to the original potential to complete a cycle (Figure 3).

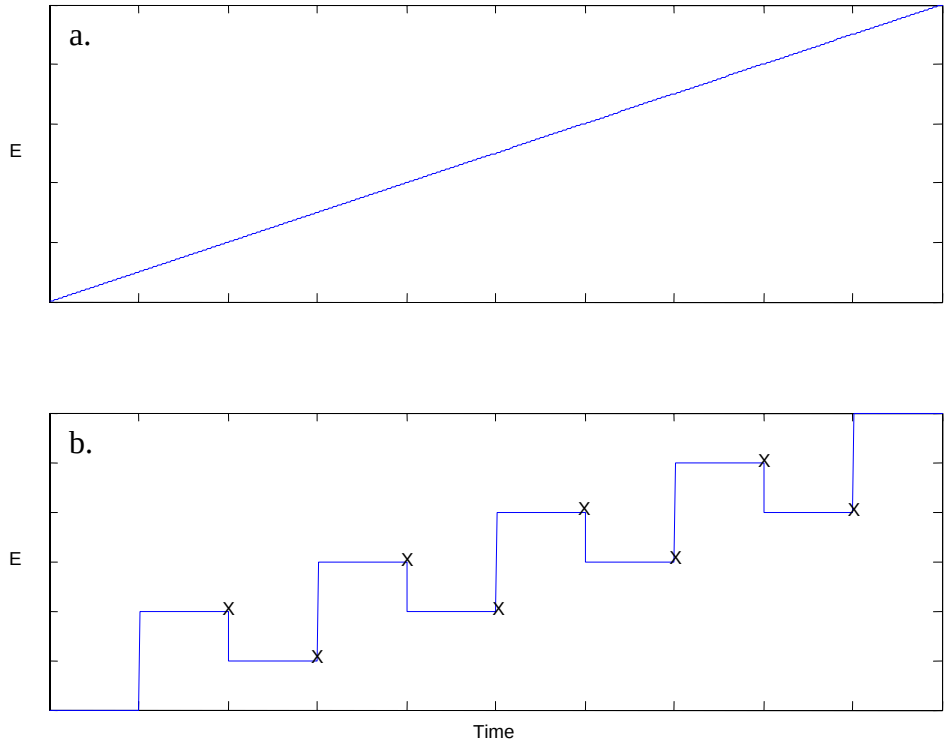

Figure 3. a. Linear (LSV) and b. square wave (SQW) potential scans used to measure O_2 (LSV), Mn^{2+}, Fe^{2+}, Organic-Fe(III), ΣH_2S, $FeS_{(aq)}$ (SQW). LSV uses a linearly-increasing potential with time. SQW uses a linearly-increasing square wave function with sampling at the end of each step, denoted by X.

Square wave voltammetry (SQW) is used for low-noise redox species detection. It has a similar potential range to LSV (~-0.1 to -1.75 V), except the potential is applied as a series of square wave modulations with pulses of equal amplitude but reversed polarity (Figure 3). Current sampling takes place at the end of each step, where potential has been steady and so the capacitance current is low. The positive and negative currents are then subtracted. As the current is equal in intensity but of reverse sign at the end of each pulse, the resulting current increases the sensitivity.

Voltint.m for use with data processing

Voltint is a Matlab-based program designed specifically to extract current intensities and surface areas of peaks for chemical species in a voltammogram. It can be used for cyclic, linear sweep, and square wave voltammetric scan techniques.

Voltint basics

At the beginning of the program, Voltint allows the user to select a group of voltammetric files to integrate. It also allows the user to select the number of points used in a moving average smoothing of the data set. Once Voltint has imported the selected files, it presents the first voltammogram of the file sequence along with its smoothed curve in a new window, which may be maximized to fill the entire screen. Voltint recognizes the file type based on the structure of the data file. Linear sweep and cyclic data files contain a column to represent the scanned potentials, and a column to represent the resulting current. Square wave data files, on the other hand, contain a column for scanned potentials, and three columns for the forward, reverse, and resultant currents.

Before the user begins the integration, they are given the chance to zoom in on the voltammogram to investigate smaller peaks. To start integration, the user depresses the START button (in the case of linear sweep, Figure 4), the NO DECONVLTN button (in the case of square wave, Figure 5), or the ANODIC/CATHODIC button (in the case of cyclic wave voltammetry, Figure 6).

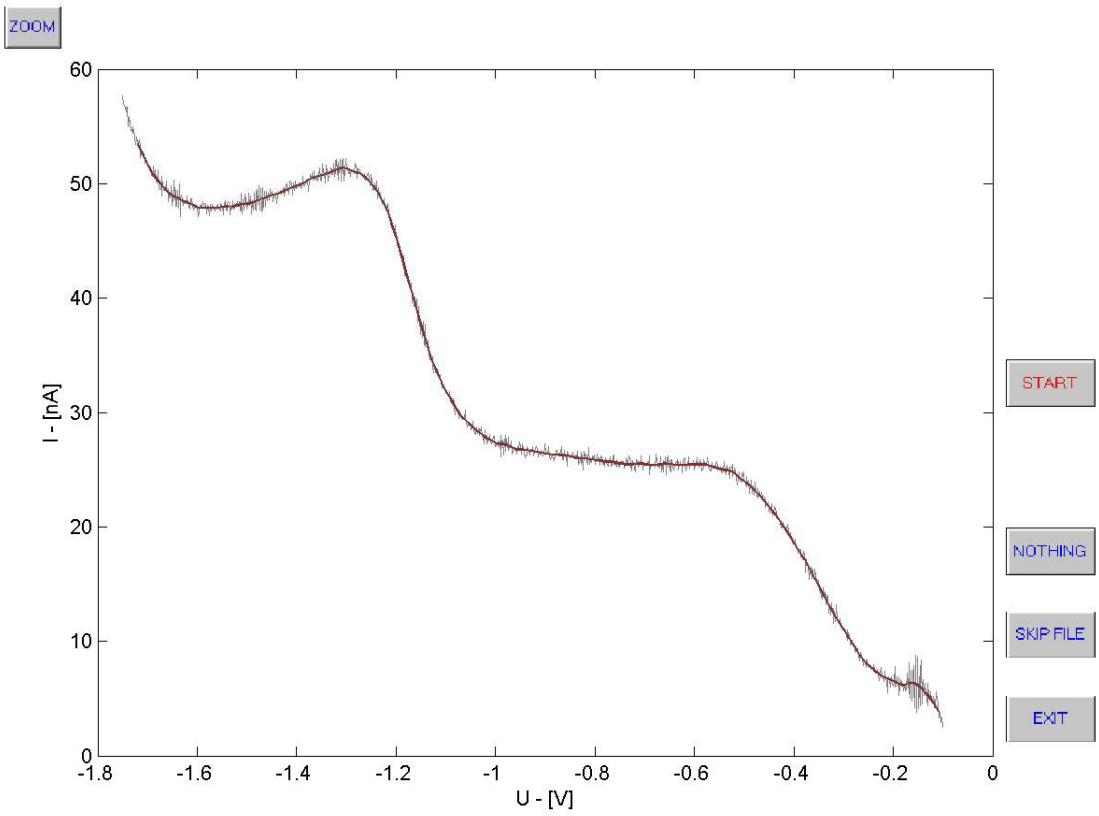

Figure 4. Example linear sweep voltammogram. Grey line: raw data, red line: smoothed data. Buttons: Upper left button for zooming in or out, on the right, in descending order: START begins the program, NOTHING signifies to the program that the voltammogram measured no redox species, SKIP FILE signifies that the file contains no meaningful information (i.e., noise or saturation) and should be skipped, and EXIT saves and exits the program.

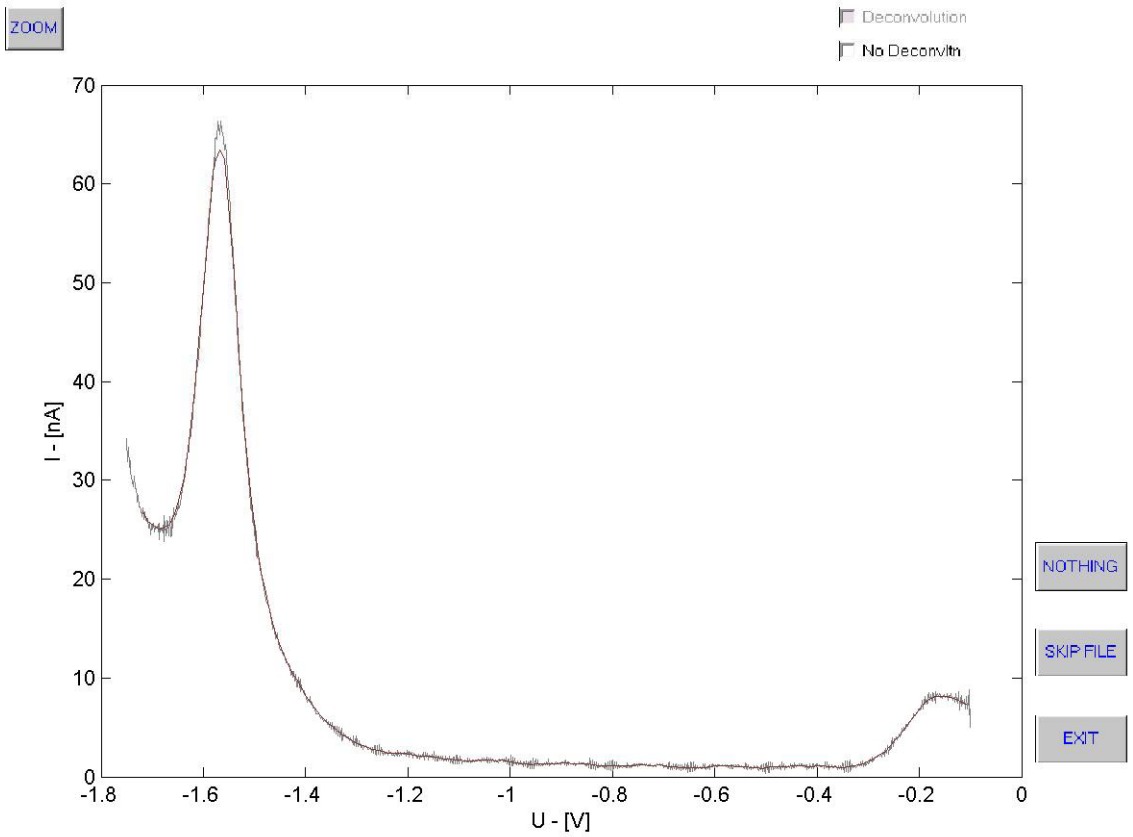

Figure 5. Example square wave voltammogram. Grey line: raw data, brown line: smoothed data. Buttons: Upper left button for zooming in or out, on the right, in descending order: START begins the program, NOTHING signifies to the program that the voltammogram measured no redox species, SKIP FILE signifies that the file contains no meaningful information (i.e., noise or saturation) and should be skipped, and EXIT saves and exits the program.

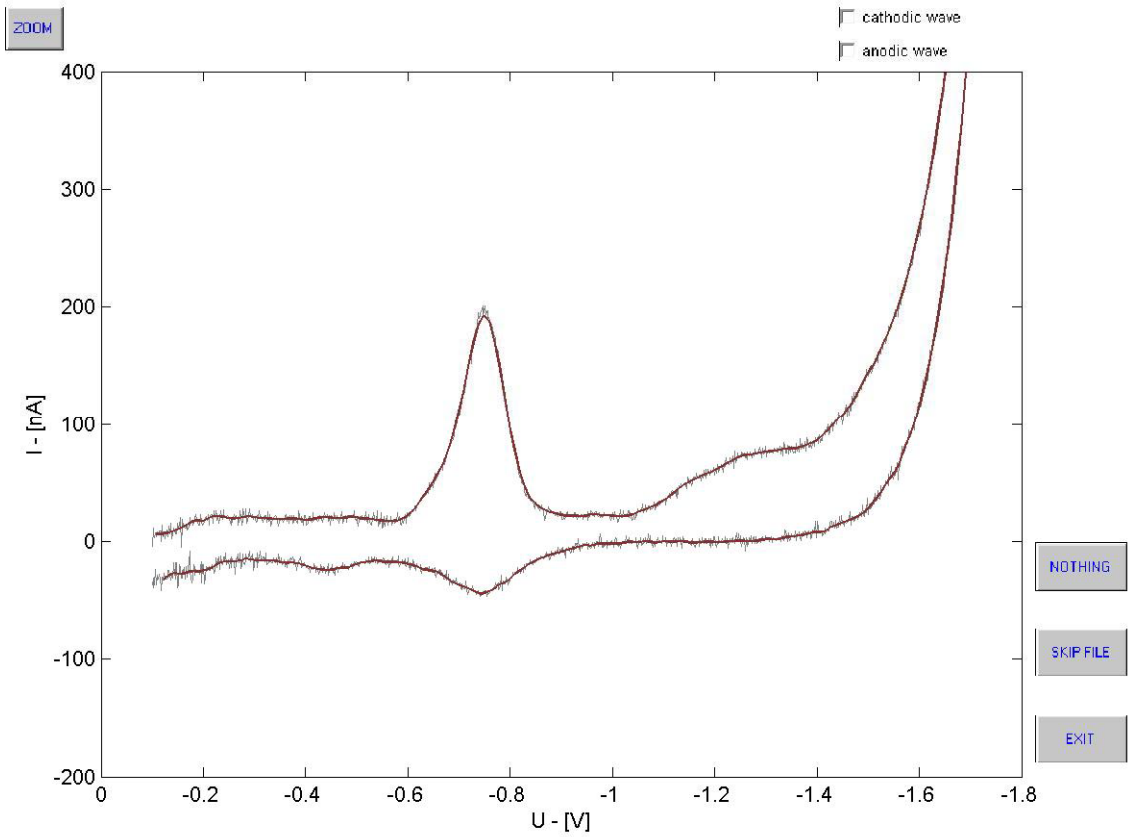

Figure 6. Example cyclic voltammogram. Grey line: raw data, red line: smoothed data. Buttons: Upper left button for zooming in or out, on the right, in descending order: START begins the program, NOTHING signifies to the program that the voltammogram measured no redox species, SKIP FILE signifies that the file contains no meaningful information (i.e., noise or saturation) and should be skipped, and EXIT saves and exits the program

These buttons initiate peak extraction by activating the GUI over the plotted data, so that the program can detect points on the voltammogram clicked by the user. To process linear sweep and cyclic voltammetry files, Voltint prompts the user to specify points above and below the wave of interest (Figure 7). After the user selects points, colored horizontal lines appear on the voltammogram delimiting the beginning and end of the wave. For cyclic voltammetric files, the user must first select the direction of the scan, as cathodic scans (in the negative direction) have waves of positive currents, while

anodic scans (in the positive direction) produce waves of negative currents (Figure 6). To select the baseline of a square wave voltammetric peak, the user clicks the data line at the base of a peak then clicks a second time on data at the other side of the peak. Colored circles are generated at the closest point on the scan to that which delimits the baseline, and a linear interpolation between the two points generates the baseline (for SQW) (LSV and CV: Figure 7 and SQW: Figure 8).

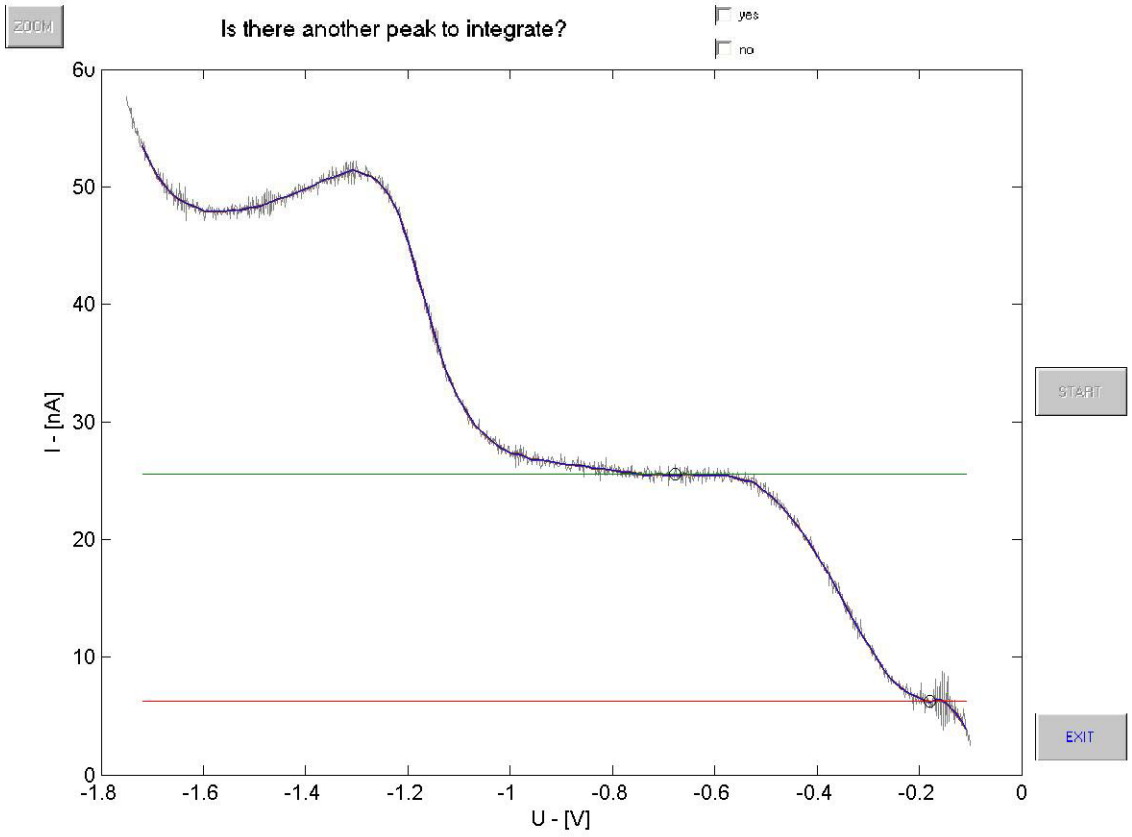

Figure 7. Example linear sweep file during processing. The blue and red horizontal lines indicate places on the scan selected by the user to act as bounds for integration.

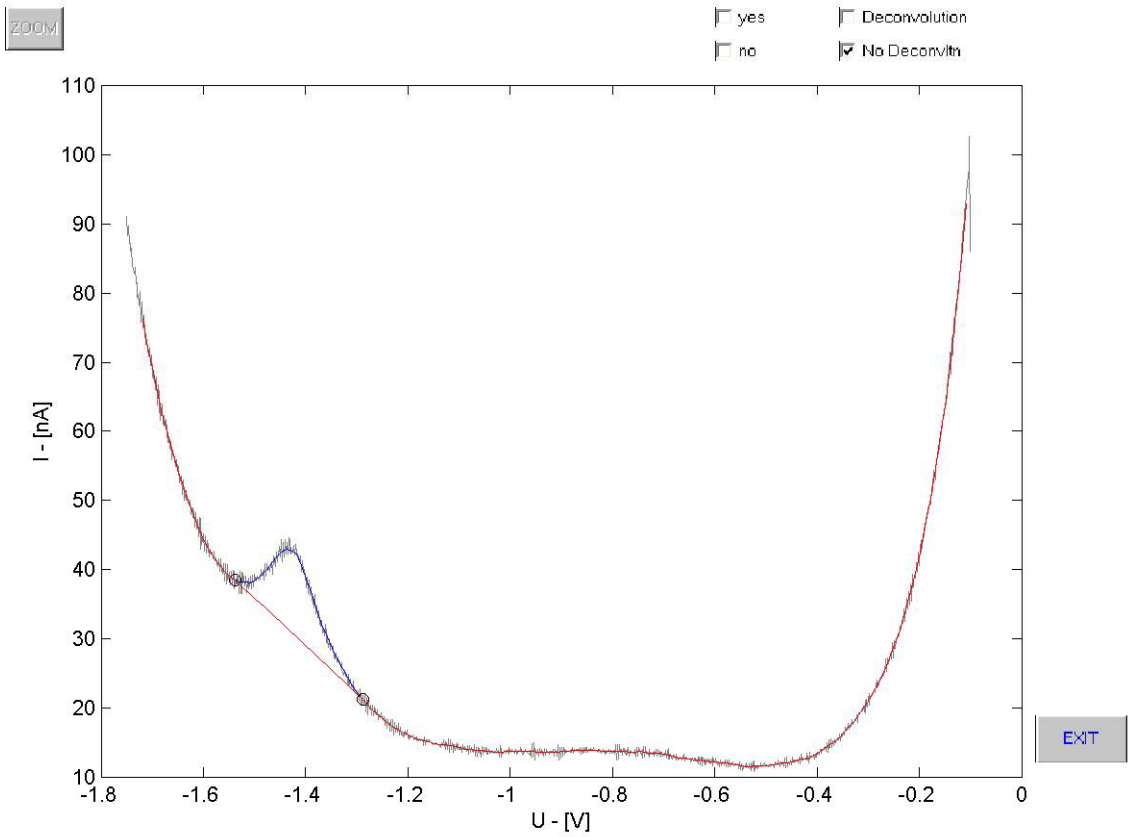

Figure 8. Example square wave voltammogram during processing. The gray jagged line is data, blue line smoothed data, and red the baseline as chosen by the user. Two small circles on the data represent the places selected by the user to act as bounds for integration.

The user is then prompted to decide whether or not the baseline is appropriate. If not, the user is allowed to redefine the baseline points. If it is adequate, then the user is prompted to decide whether or not to integrate another peak in the same scan. If it is the case, the baseline definition process is reiterated. If the user is finished with the file, Voltint saves the information selected by the user, closes the file, then opens the next file in the sequence.

The user may bypass any scan by depressing the SKIP button on the right hand side of the plot, which makes a note in the output file that the scan contained no useful

information. Or, if the scan is of good quality but the measurement indicates that there are no redox chemical species detected in solution, the user may depress the NOTHING button, also on the right, which makes a note in the output file and then skips to the next file in the sequence.

When the sequence is finished, the program saves the output to ASCII text files and exits. The program makes two types of output files of the form pkSW##_##.txt or SQW##_###.txt (both for square wave), where ## indicate the numbers of the first and last files in the processed sequence. The pk file contains columns for the file number, the potential where a peak was processed, the peak height, and the peak area. The SQW file contains columns for the scanned potential, and the resultant currents. In the case of a SKIP, the corresponding row in the pk file contains the file number, then NANs for all the other columns. In the case of a file where the user depressed the NOTHING button, the output row contains the file number, then all zeros in the other columns.

Voltint calculations

Once the region to integrate is specified by the user, Voltint determines the height of the selected peak, then the potential at half-height, which helps the program identify the species. The potential at half-height is determined by taking the derivative of the selected curve and finding the potential corresponding to the maximum of the derivative current.

To process a square wave file, once the baseline has been identified by the user, Voltint finds the potential at which the current is at maximum height. Height is defined as the distance between the baseline and the maximum point on the selected peak. This is

the magnitude of the current at the highest point. To find the surface area under the peak, Voltint uses the trapezoidal rule.

Square wave processing offers the user the chance to deconvolve overlapping peaks. To choose NO DECONVOLTN bypasses the deconvolution option.

Deconvolution

Sometimes, redox chemical species produce square wave voltammetry peaks that overlap. This is common for Fe^{2+} and Mn^{2+}, which produce voltammetric peaks at approximately -1.4 and -1.55 V, respectively. In the case of such a problem, it is necessary to deconvolve the voltammetric peaks. A subroutine was written to deconvolve peaks for square wave voltammograms, either in the anodic or cathodic direction.

The subroutine can be called for each voltammogram using a click button ('deconvoltn'). Once this selection is made, the program enters the subroutine (process.m). The user is prompted to select the region on the voltammogram where the convoluted peaks are located to process with the deconvolution. Once the region is identified, the smoothed voltammogram is inspected automatically to find the different modes available. The second derivative of the current is used to find the potentials of the modes that will define the convoluted peak. A default threshold current is used to identify peaks. This threshold current is not adjustable for now. If the voltammogram is cathodic (i.e., positive currents), the maxima of the second derivative above the threshold current will provide the number of peaks and their potential. If the voltammogram is anodic (i.e., negative currents), the minima of the second derivative below the threshold current provide the number of peaks and their potential.

Once the modes have been identified, the program interpolates the baseline below the peaks assuming a linear regression between the potentials selected by the user. Once the baseline is created, the program enters subroutines to generate gaussian curves through each mode using the following equation:

$$I = I_{1/2} \cdot \exp\left(-\frac{1}{2}\left(\frac{E - E_{1/2}}{w}\right)^2\right) \qquad 1$$

where $I_{1/2}$ and I are, respectively, the maximum current and the current of the peak, $E_{1/2}$ and E are, respectively, the half-wave potential and the potential of the peak, and w is the width of the peak at half-height.

To generate these gaussian curves, guesses are provided for all the parameters of the right-hand-side of equation (1) except the potential and the half-wave potentials, which are known. The maximum current is guessed to be the current of each mode, while the half-width potential is guessed to be 150 mV, typical for one- or two- electron transfer reactions. Once the gaussian curves are calculated, the program uses the 'lsqnonlin' function of Matlab, which solves non-linear least squares problems, to minimize in a least-square fashion the difference between the measured curve and the sum of the baseline currents and the individual gaussian peaks. The parameters optimized are the peak maximum current ($I_{1/2}$), the half-wave potential width (w) and the baseline. Once optimized, the error is compared to the noise of the voltammogram. If the error is greater than the noise, a flag is raised to warn the user that the calculation might not be accurate. The deconvolution program returns the deconvolved peaks half-wave potentials, currents, and surface area information to the calling function. It also displays, superimposed to the rawdata and smoothed curve, the reconstructed voltammogram

within the region containing overlapping peaks and peak heights corresponding to the modes.

Water Level Sampling

To investigate the rate and direction of the local tide, four wells were installed at the tidal creek approximately 3 feet upstream from the sampling point. Leveloggers (Solinst) were placed in the wells to measure the water pressure as a function of time, while a barologger (Solinst) was deployed to measure the atmospheric pressure over multiple tidal cycles. Water levels in the wells were determined by subtracting the atmospheric pressure from the water level readings. Each of the four wells contained a 5 cm screen located at approximately 0, 15, 30, and 60 centimeters deep into the sediment, respectively (Figure 9).

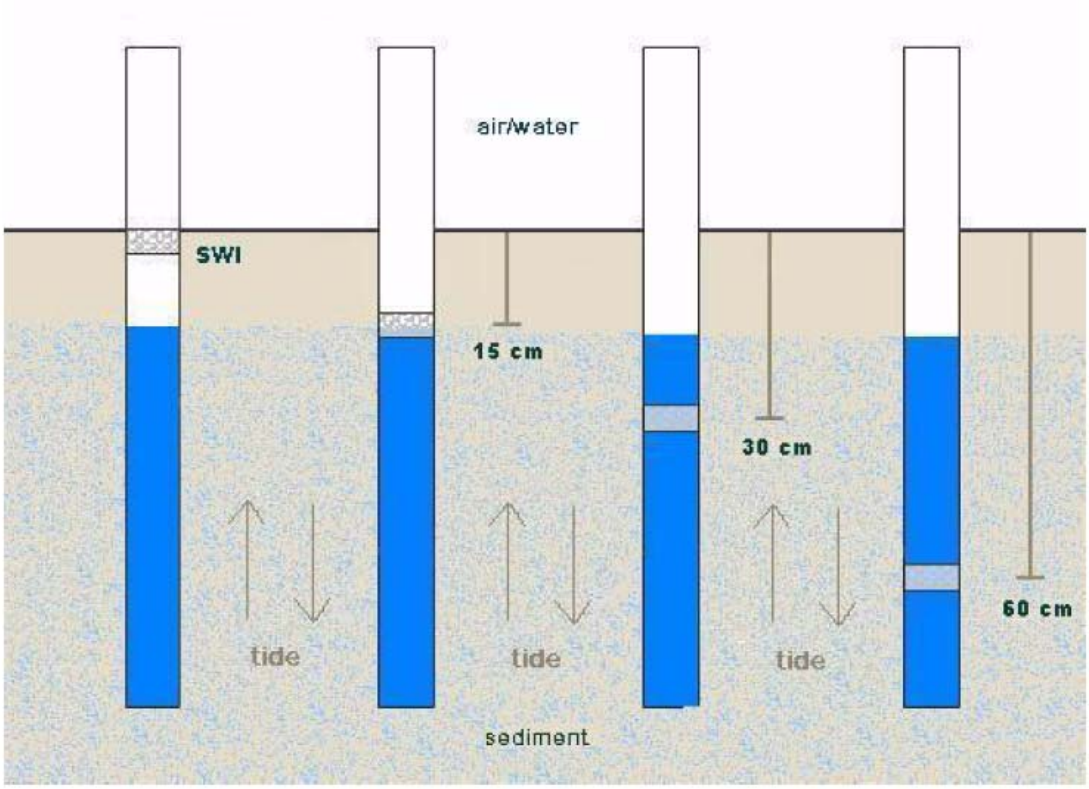

Figure 9. Well diagram: Wells were placed in the salt marsh tidal creek 3 feet from the sampling site. Four wells were installed 30 cm apart, with screens at 0, 15, 30, and 60 cm deep in the sediment. Water level measurements were performed with Levelloggers (Solinst).

Mathematical Model

A transient, reactive transport model was built in Matlab® to simulate depth profiles of oxygen, solid phase ferric iron, ΣH_2S, and ferrous iron in salt marsh sediment over time. The model shows the effects of advection, microbial and chemical reactions, sedimentation, bioturbation, and chemical diffusion on the geochemistry of the sediment. The objective of the model is to investigate if the tides play a major role on biogeochemical processes in salt marsh sediments, specifically with regard to iron cycling.

The model calculates numerical approximations to the transient reactive advection-dispersion equation in one dimension to describe changes in chemical concentrations with depth (Eq. 2):

$$\frac{dC}{dt} = D\frac{d^2C}{dz^2} - v\frac{dC}{dz} \pm R \qquad 2$$

Where C represents chemical concentration, z: depth (cm), t: time (min), v: sedimentation rate (cm/min) for solid phase and advection rate for dissolved phase, and D: dispersion coefficient for solutes and diffusion coefficient due to bioturbation for solid phases (cm^2/min). In this instance, bioturbation loosely refers to any biological activity which mixes the sediment. R represents chemical reactions.

To ensure stability, the model incorporated a method that uses a central finite difference in space and a Crank-Nicolson scheme in time (Boudreau 1997). The Strang-splitting method (Strang 1968, Zysset and Stauffer 1992) was employed to minimize instability created by the large advection found in salt marshes. This method centers the reaction step between two transport steps for each time increment.

The model was calibrated to simulate salt marsh tidal creek conditions. It represents 10 cm of sediment, has an advection of 0.5 x 10^{-2} $^{cm}/_{min}$ and simulates fifteen days to mimic in-situ time series electrochemical profiles. Spatial step sizes were determined using the Peclet number (Boudreau 1997) and error analysis, while time steps were determined using the Courant number (Boudreau 1997) to help ensure that the model was stable and accurate.

The initial condition for all chemical species in the sediment is zero at all depths, excluding the boundaries: the very top of the domain, representing the SWI, and the bottom (depth of sediment). Dirichlet boundary conditions were set at the sediment-water interface for oxygen and solid iron. The iron oxide concentration was fixed to zero, but the oxygen concentration varied sinusoidally with the tides (Figure 10). Real tidal periods were used to determine oxygen variations, with a maximum O_2 concentration of 250 μM to simulate oxygen saturation in the overlying water at low tide, and a minimum oxygen concentration set to 90% of saturation during high tide. ΣH_2S and Fe^{2+} have a zero flux boundary (Neumann boundary) at the SWI. At the bottom boundary, Fe^{2+} is set to 300 and ΣH_2S to 1500 μM to simulate sulfate reduction deep in the sediment and its effect on the reduction of iron oxides. At this depth, O_2 and Fe-oxide have a zero flux boundary.

In the model, sedimentation and porewater advection vary sinusoidally to reflect tidal influences (Figure 10). Advection is forced to flow out of the sediment during flood tides and into the sediment during ebb tides. Sedimentation is zero for low tide, and is at a maximum during high tide. The phase of the tide simulated in the model matches that of the semidiurnal tide measured in the field (See Figure 10).

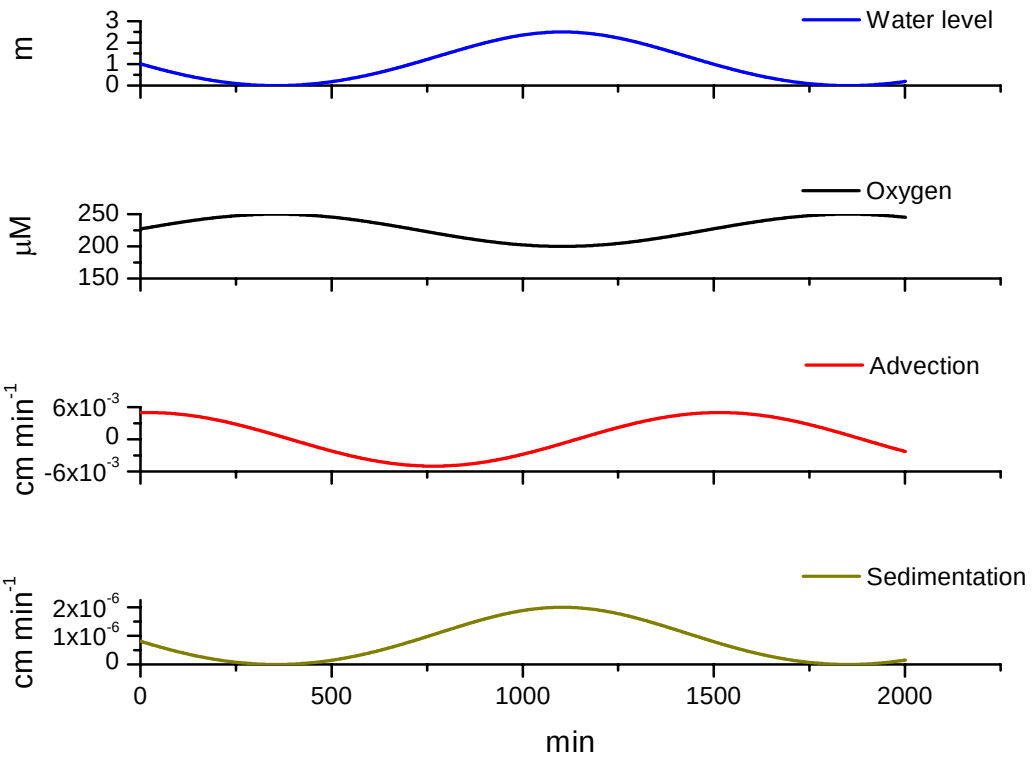

Figure 10. Tidally-affected parameters used in the model. Blue: simulated water level due to the tide, black: dissolved oxygen concentration at the SWI, red: porewater advection (where positive refers to water movement into the sediment from above), and green: sedimentation of $Fe(OH)_3$.

The model simulated some of the biogeochemical reactions in Table 1 using kinetic rate laws obtained from literature. These reactions were built into the model as in Table 2. $Fe(OH)_3$ is created from abiotic oxidation of Fe^{2+} (Stumm and Morgan 1996), and is reductively dissolved by FeRB (Kostka et al. 2002) and by reaction with dissolved sulfide (Yao and Millero 1996). Fe^{2+} is produced and removed from the reduction and production of $Fe(OH)_3$. Fe^{2+} is also removed by $FeS_{(s)}$ precipitation (Rickard 1995). Hydrogen sulfide is created by SRB activity (Kostka et al. 2002) and is removed by

oxidation by O_2 (Millero 1987), precipitation of $FeS_{(s)}$, and reduction of $Fe(OH)_3$.

Oxygen is consumed by the above reactions as well as by aerobic respiration.

Table 2. Overall reaction rate laws used in the model to represent sources and sinks of $Fe(OH)_3$, Fe^{2+}, O_2, and ΣH_2S due to microbial and abiotic reactions. Rate laws were obtained from the literature, when possible. k_{ox} is the oxidation rate constant of Fe^{2+} by O_2, k_{FeRB} is the reduction of $Fe(OH)_3$ by FeRB, k_{rfes} is the dissolution and reduction of $Fe(OH)_3$ by ΣH_2S, k_{rfe2s} is the precipitation of Fe^{2+} and ΣH_2S to $FeS_{(s)}$, k_{os} is the oxidation of ΣH_2S by O_2, k_{ar} is aerobic respiration, and k_{srb} the reduction of SO_4^{2-} by SRB.

$$\frac{d[Fe(OH)_3]}{dt} = 4\frac{k_{ox}[O_2][Fe^{2+}]}{[H^+]^2} - k_{FeRB}[Fe(OH)_3] - k_{rfes}[\Sigma H_2S][Fe(OH)_3]$$

$$\frac{d[Fe^{2+}]}{dt} = k_{FeRB}[Fe(OH)_3] - k_{rfe2s}[\Sigma H_2S][Fe^{2+}] - 4\frac{k_{ox}[O_2][Fe^{2+}]}{[H^+]^2}$$

$$\frac{d[O_2]}{dt} = -\frac{k_{ox}[O_2][Fe^{2+}]}{[H^+]^2} - \frac{1}{2}k_{os}[O_2][\Sigma H_2S] - k_{ar}[O_2]$$

$$\frac{d[\Sigma H_2S]}{dt} = k_{srb}[SO_4^{2-}] - k_{os}[O_2][\Sigma H_2S] - k_{rfe2s}[Fe^{2+}][\Sigma H_2S] - k_{rfes}[Fe(OH)_3][\Sigma H_2S]$$

Table 3. Constants used in the model. Physical parameters: bioturbation: refers to mixing of sediment as a result of biological activity, sedimentation: $Fe(OH)_3$ from the overlying water, advection: tidally-induced porewater advection through the sediment. Chemical parameters: as illustrated in Table 2.

Table 3. Constants used in the model	
Bioturbation	1×10^{-6} cm^2 min^{-1} [Berner, 1980]
Sedimentation	2×10^{-6} cm min^{-1} [Berner, 1980]
Diffusion	1.4×10^{-3} cm^2 min^{-1} [Berner, 1980]
Advection	1×10^{-2} cm min^{-1} sensitivity analysis
Oxidation of Fe^{2+} by O_2	3×10^{-11} M^{-1} min^{-1} [Stumm and Morgan, 1996]
Oxidation of ΣH_2S by O_2	1×10^{-23} M^{-1} min^{-1} [Millero, 1987]
Reduction of iron oxide by FeRB	1×10^{-3} M^{-1} min^{-1} [Kostka et al., 2002]
ΣH_2S reduction of iron oxide	1.48×10^{2} M^{-1} min^{-1} [Yao and Millero, 1996]
Precipitation of Fe^{2+} by ΣH_2S	1×10^{-7} min^{-1} sensitivity analysis
Sulfate reduction by SRB	1.25×10^{-7} min^{-1} [Kostka et al., 2002]

Rate constants and physical parameters used in the model were taken from literature whenever possible (Table 3). Other values were obtained through sensitivity analysis.

Mass balance calculation

The model was tested for mass balance. The Matlab® function built to perform this calculation used model output to calculate changes in simulated concentration of the species of interest as a result of transport and chemical reactions. The calculation was

made using flux of the species in and out of the model, according to the following schematic:

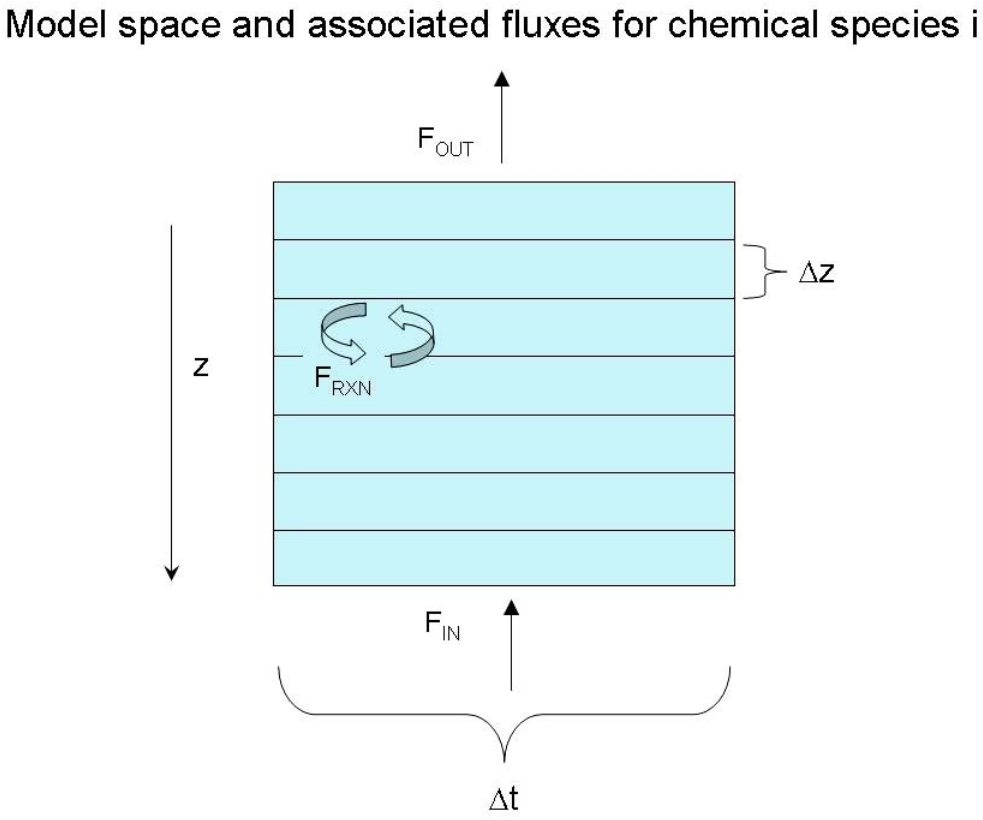

Figure 11. Diagram for mass balance calculation. F_{IN} is the flux of species into the model space, F_{OUT} is the flux of that species out of the model space, F_{RXN} is the flux of the species out of the model space by means of chemical reactions, z is depth, Δz is a space step, and Δt is a time step.

$$F_{IN} + F_{OUT} + F_{RXN} = 0$$

Where z is depth, Δz is a space step, Δt is a time step, F_{IN} is the flux of species into the model space, F_{OUT} is the flux of that species out of the model space, and F_{RXN} is the flux

of the species out of the model space by means of chemical reactions (for example, Fe^{2+} may react to form an Fe-oxide, which effectively takes Fe^{2+} out of the model space). Here, F_{IN} and F_{OUT} are defined according to Equation 3:

$$F_{IN/OUT} = 0.001\left(-D\frac{dC}{dz} + uC\right) \qquad 3$$

Where D is dispersion, u is advection, and 0.001 converts L to cm^3. Generally, in this calculation, the flux of a species leaving the model space is subtracted from the flux of that species that comes in from the opposite side (i.e., the amount of a species leaving from the model at depth = 0 is subtracted from the amount that enters from depth = 10 cm, which is the deepest part in the model domain). This calculated difference in a species' flux is compared to the change in flux of that species as a result of reactions simulated to take placed within the model space. If the difference in a species flux from entering to leaving the model cannot be accounted for by reactions taking place within the model space, then the model is not mass balanced. This is a relatively simple calculation because the model is one dimensional with respect to space.

To calculate the effects of chemical reactions on the fluxes of the chemical species, the function increments through time steps, and at each one calculates the reaction rates that take place at each depth in the model, leaving a matrix of concentrations for each time step. After these calculations are complete, the function then sums all of the changes in concentration over depth, leaving a vector of numbers whose individual values represent the overall effect of chemical reactions on the concentration of the species of interest over the entire spatial domain at each time step.

In summary:

$$F_{RXN} = 0.001\int_{0}^{L} \frac{dC}{dz} dz \qquad 4$$

Finally, the function compares the change in flux due to transport in and out of the model space to the change in flux from chemical reactions. The difference represents the degree to which the model is not mass balanced.

CHAPTER 3

RESULTS

Core chemical profiles

Core 1 (Figure 12) was taken at low tide, with a temperature of 27.6 ˚C, salinity 33 ppt. This chemical depth profile exhibits a maximum Fe^{2+} concentration at 10 mm depth in the sediment. Dissolved Fe^{3+} reaches a maximum of 80 μM at 15 mm. Amorphous iron oxides reach a maximum of 72 μmole/g between 5 and 10 mm. These concentration profiles show overlapping maxima of Fe^{2+}, dissolved Fe^{3+}, and amorphous Fe-oxides, which is counterintuitive for a steady-state system. In the expected steady-state profile, oxidized iron would reach a maximum near the SWI, reduced dissolved iron would reach a maximum in the anoxic zone (below the oxidized iron), and there would be a shortage of iron at depth where $FeS_{(s)}$ precipitation is expected. Apparently this system is not at steady state; The data further suggest abiotic or microbial reduction of Fe-oxides near the SWI or transport of reduced iron from deep in the sediment. Other core profiles from the same location (Figure 13) show similar overlap of Fe^{2+} and Fe^{3+}.

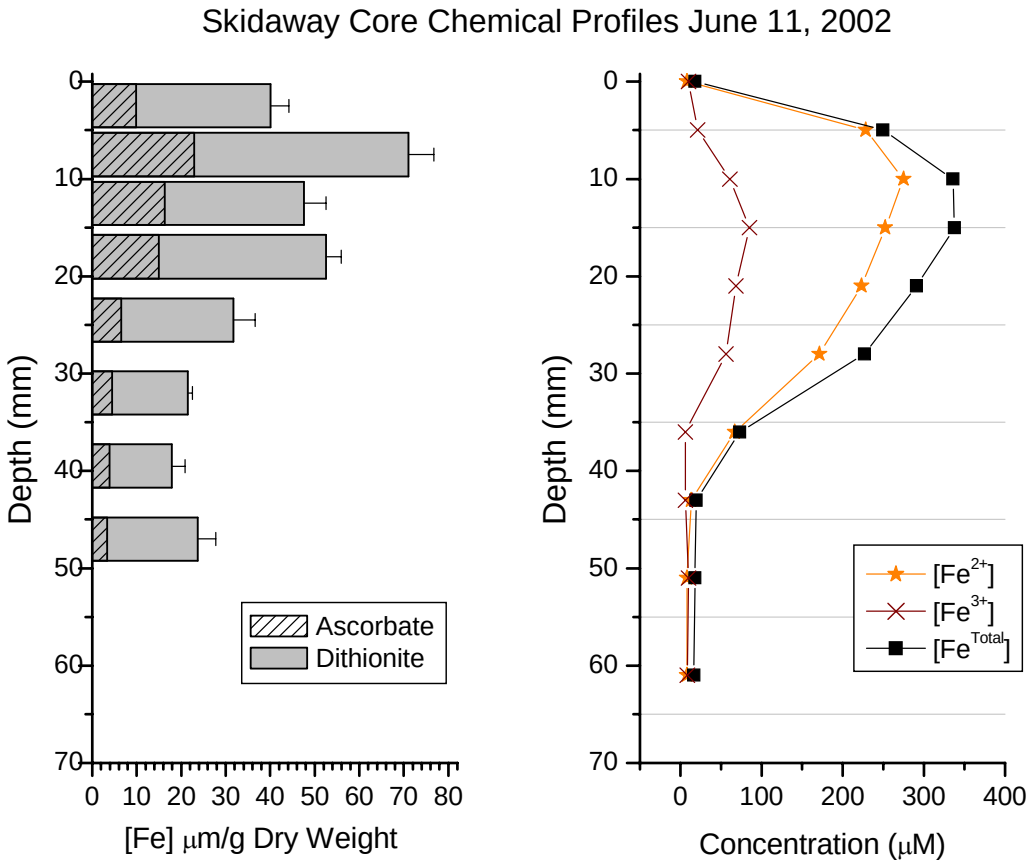

Figure 12. July 11, 2002 sediment core profiles. Left: A depth profile of solid iron oxides in the sediment. Solid bars represent crystalline iron oxides and AVS, and striped bars are amorphous iron oxides. Right: Core porewaters with Fe_{Total} (black squares), Fe^{2+} (orange stars), and Organic-Fe(III) (red x's).

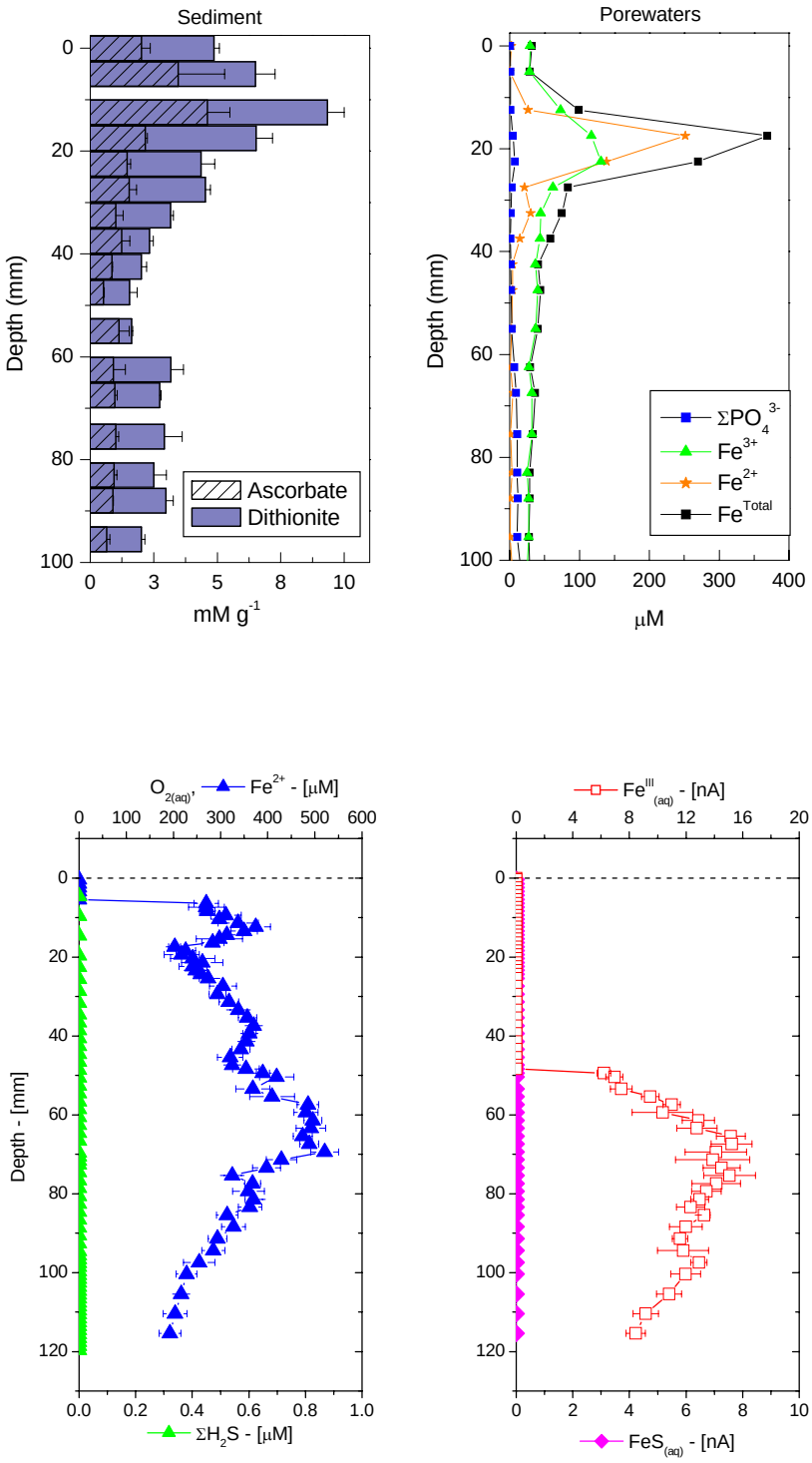

Figure 13. Top: geochemical core profile of intertidal salt marsh creek bank sediment at SKIO taken June, 2003. Bottom: voltammetry core profile taken at same location July, 2004.

Well data

Water levels from the salt marsh monitoring wells were compared to water levels obtained by a NOAA buoy at Ft. Pulaski, GA, approximately 30 miles away. The comparison shows a lag of approximately 1 hr and 48 minutes from Ft. Pulaski to the sampling site (Figure 14).

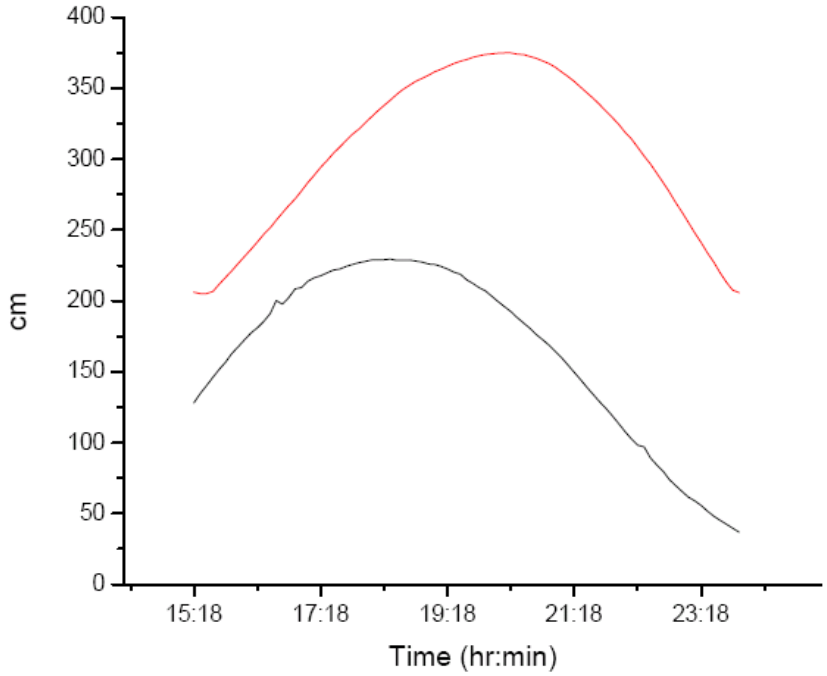

Figure 14. A time comparison of high tides between water levels in the local wells and water levels above the sediment from a NOAA buoy at Fort Pulaski, GA. High tide at the salt marsh (red, upper line) lags behind the NOAA buoy (black, lower line) high tide by 1:48 hrs.

Well water level data measured in June and September, 2003 (Figure 15 & Figure 16) show a delay between wells. Wells with deeper screens began to fill before the shallower wells. These results imply that during flood tide, water advects through the

sediment rather than flows over the top of the sediment. Linear fits to the difference between well water levels were made to find an average velocity for tidally-induced advection from screen to screen. In well water data taken during the June, 2003 sampling, advection from well B6 (with a screen ~15 cm into the sediment) to well B0 (at the sediment-water interface) was calculated to be approximately 47 and 53 cm/hr for the two flood tides, respectively. From the September, 2003 sampling, average advection from well B6 to well B0 was 23 cm/hr. Advection from the September B12 well (~ 30 cm into sediment) to B0 was 26.5 cm/hr and 26.6 cm/hr for the two flood tides, respectively. Differences between the June and September well advection calculations may be accounted for by a lag in the September data, which may have been due to detritus from *Spartina alterniflora* that collected at the SWI well screen over the three months following well installation, or from sediment that may have accumulated at and clogged the well screen.

Additional advection calculations were made using Darcy's Law (Taillefert et al, 2006):

$$v_z = -K\frac{dh}{dz} \qquad 5.$$

Where K is hydraulic conductivity (cm s^{-1}), dh is the well water level difference (cm), and dz is distance between well screens (cm). These calculations yielded maximum advection rates of 15-20 cm hr^{-1}.

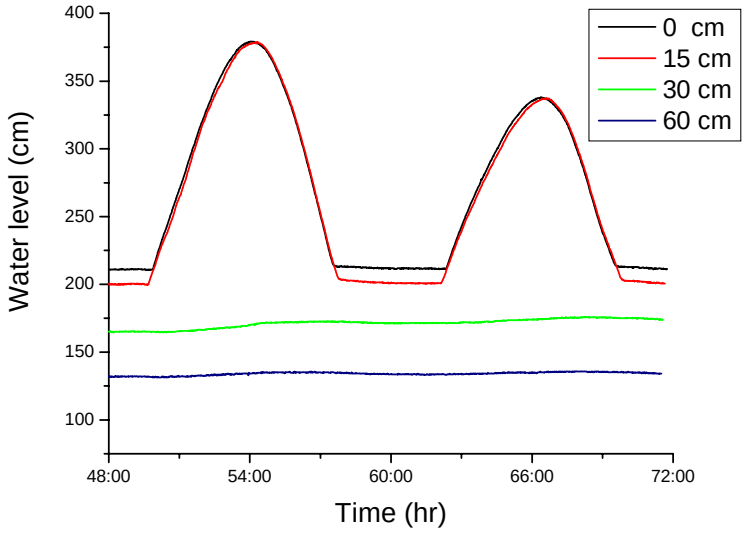

Figure 15. Salt marsh tide water levels obtained from monitoring wells with screens located at 0, 15, 30, and 60 cm below the SWI in June, 2003.

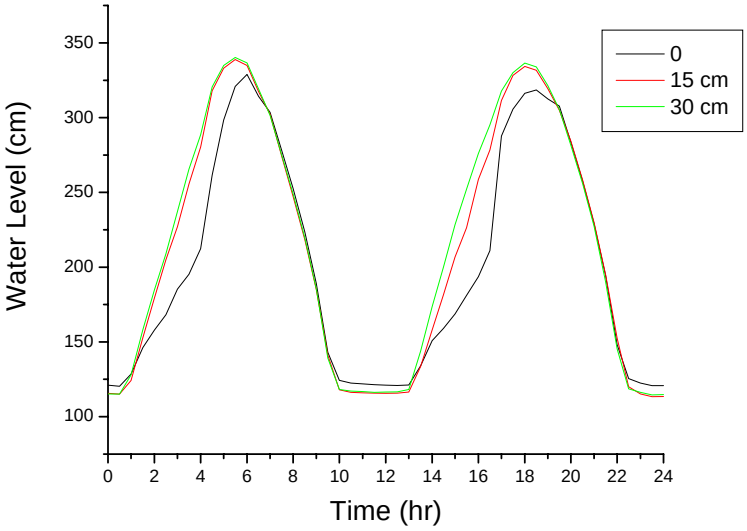

Figure 16. Salt marsh tide water levels obtained from monitoring wells with screens located at 0, 15, and 30 cm below the SWI in September, 2003.

June 28, 2003 time series data

June 2003 electrochemical measurements (Figure 17) were performed for approximately one tidal cycle. Tidal data were taken from Ft. Pulaski, with a lag included to show the monitoring wells at the sample site. Five electrodes were used in this measurement: in the overlying water, at 0, 3.5, 7, and 10.5 cm deep into the sediment. During the first low tide event measured, reduced iron appeared in the overlying water. At approximately 17:00 hrs, reduced iron decreased both in the overlying water and at the sediment water interface, so that by 18:00 hrs its concentration was approximately zero. Meanwhile, soluble organic-Fe(III) reached a maximum at 17:00 hrs in the overlying water. At the SWI, soluble organic-Fe(III) and Fe^{2+} had over-lapping maxima at approximately 17:00 hrs, and were followed by disappearance of Fe^{2+} and production of soluble organic-Fe(III) at high tide, between 19:30 and 23:00 hrs. This peak overlap of reduced and oxidized Fe species suggests that advection in this sediment is extremely fast.

At 3.5 cm depth, ΣH_2S reached a maximum at low tide, as expected, then decreased until it disappeared completely by 18:00 hrs. Meanwhile, $FeS_{(aq)}$ at 3.5 cm deep reached a maximum at 18:00 hrs, implying that ΣH_2S was converted to $FeS_{(aq)}$ and that some Fe^{2+} must have been produced through transport or local reactions. A small amount of $FeS_{(aq)}$ was observed at the SWI at 18:00 hrs as well. Perhaps Fe^{2+} found in the overlying water drained back into the sediment during ebb tide and precipitated $FeS_{(s)}$ on its way through the sediment. Fe^{2+} and ΣH_2S both appeared in the overlying water at different times (Fe^{2+} between 12:00 and 17:00 hrs and then dropped in concentration as ΣH_2S ascended) but overlapped at about 18:00 hrs, exactly when a small $FeS_{(aq)}$ peak was

found at the SWI. At 3.5 cm, Fe^{2+} was probably removed by $FeS_{(s)}$ precipitation upon advection of ΣH_2S, as suggested by the rise in $FeS_{(aq)}$ found at 11-12:00 hrs. ΣH_2S was produced again during the next ebb tide, at approximately 24:00 hrs. It was also produced at 7 and 10.5 cm, and reached a maximum at low tide. This suggests upward advection of deep reduced porewaters that may have brought reduced metabolites to the SWI.

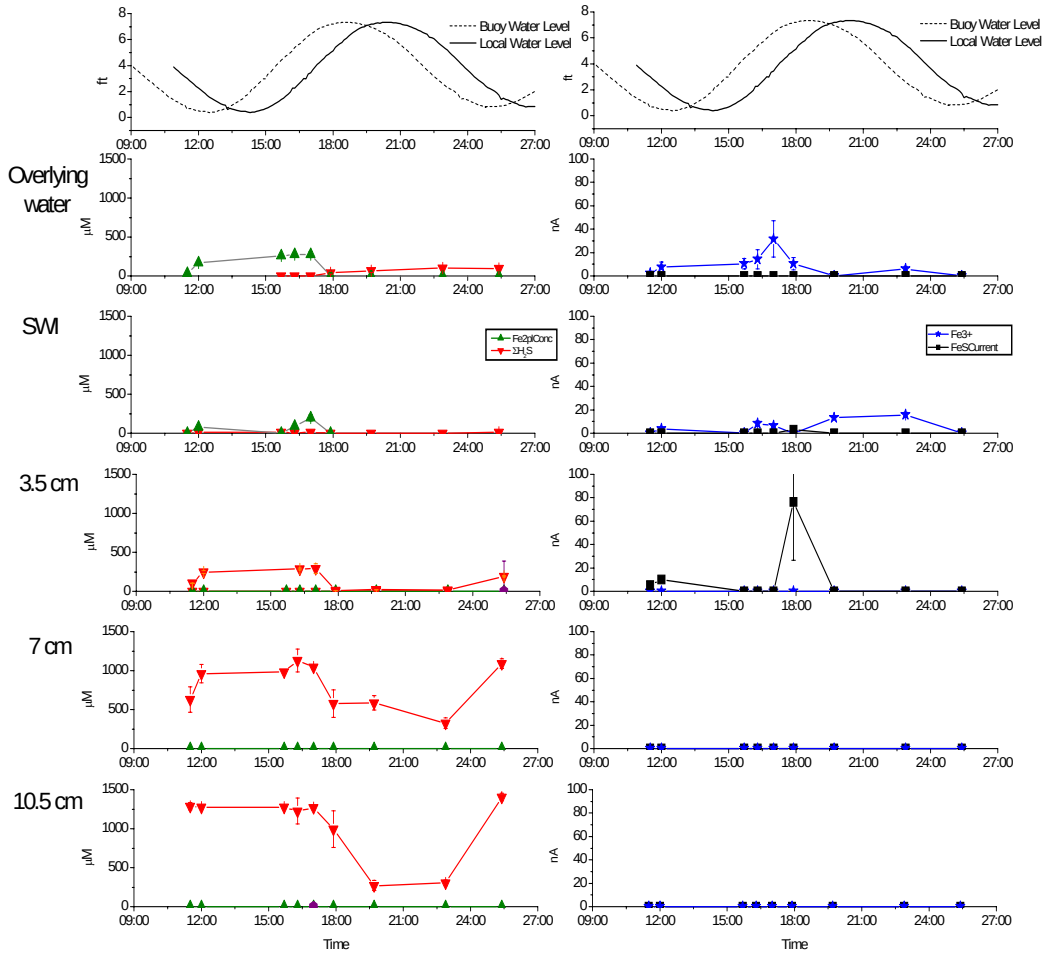

Figure 17. Voltammetric in-situ time series measurements of porewater chemical composition obtained between 11:30 AM June 26, 2003 and 1:30 AM June 27, 2003. The two matching graphs on the top display water level measured at the Fort Pulaski NOAA buoy (dotted line) and the same water level data with a lag of 1:48 hrs to represent the salt marsh tide (solid line).

July 10-12, 2004 SUB time series data.

July, 2004 electrochemical time series profiles (Figure 18) were performed for slightly more than one full tidal cycle. Three electrodes were used, placed at the SWI, 7 cm, and 11 cm deep in the sediment. The submersible potentiostat was used for this deployment, as evidenced by consistent frequency of sampling events. Each sample shown in the figure is an average of multiple voltammetric scans taken in sequence over the course of 5 minutes. Overall, each electrode produced an average measurement every 30 minutes.

Figure 18 c & d show the voltammetric measurements of an electrode set at the sediment water interface. During high, ebb, and flood tide, there is a surplus of Fe^{2+} at this electrode, with very high concentrations occurring at the second flood tide. Organic Fe(III) complexes develop during the ebb tide and increase to a peak during low tide. When the tide floods, the abundance of this complex drops to zero. At the exact same time, $FeS_{(aq)}$ is rapidly produced at the SWI, in concert with Fe^{2+}. However, neither of these happen significantly during the first flood tide. On a much smaller scale (see Figure 18c), Mn^{2+} appears at 250 μM during the first rising tide, and sulfide appears during the second at 250 μM.

At 7 cm, sulfide appears rather sporadically, but does seem to consistently peak during both low tides. It remains at a relatively low concentration (< 100μM). $FeS_{(aq)}$ and Fe(III) rise and drop during the first flood and high tide.

At 11 cm, sulfide is fairly constant at 50 μM. It rises, however, to 75 μM during low tide. At the same time, $FeS_{(aq)}$ is relatively constant until it rises at low tide.

Using voltammetry, Taillefert et al. (2000) found that fresh organic-Fe(III), formed from oxidation of Fe^{2+} in the presence of O_2 and an organic ligand, displayed a voltammetric signal at ~-0.3 volts. Older organic-Fe(III) complexes (which are probably aggregates) occurred at a more negative potential. In the July, 2004 data, we measured organic-Fe(III) at ~-0.30 volts at the SWI, -0.38 volts at 7 cm depth, suggesting that the top organic-Fe(III) was freshest while the deeper organic-Fe(III) was more aged, and thus more aggregated (Taillefert et al. 2000). However, because the nature of the ligands in these complexes is unknown, the age of these organic-Fe(III) species is uncertain.

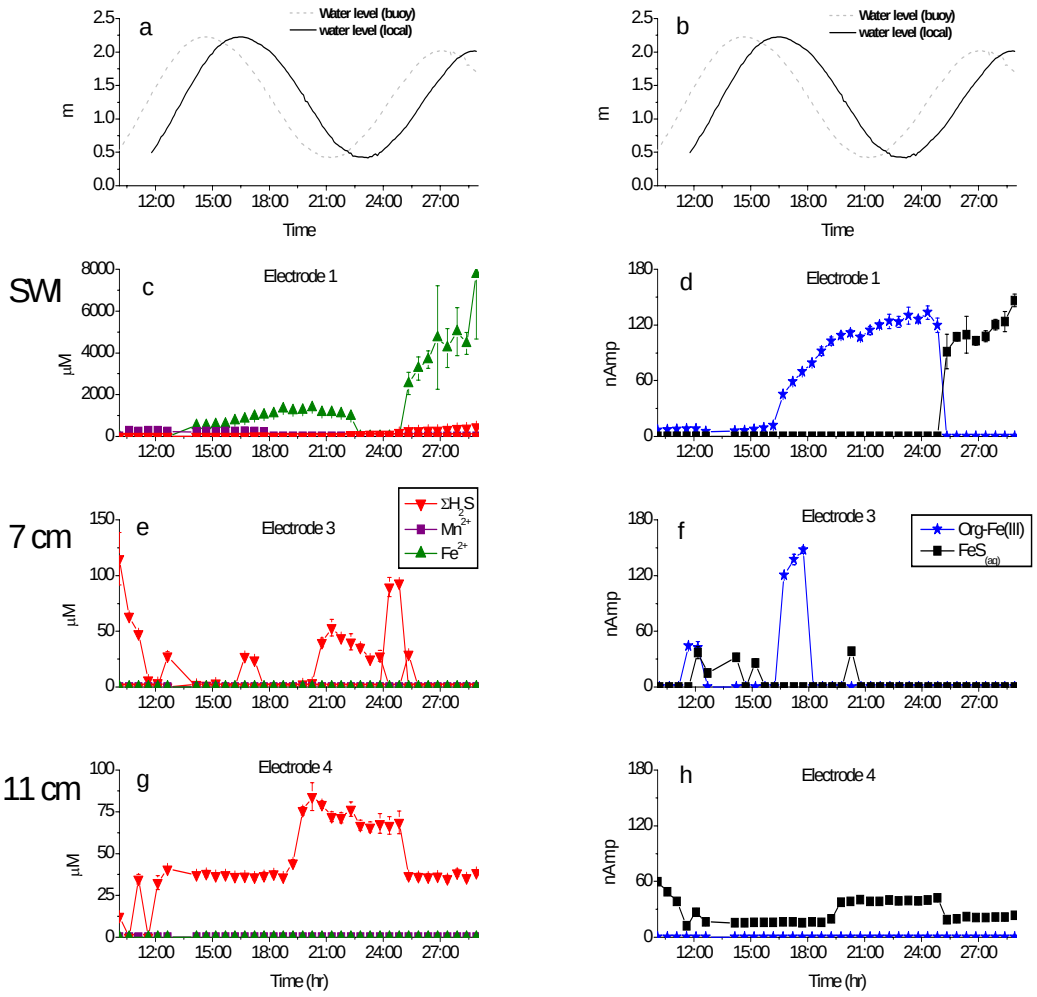

Figure 18. Voltammetric in-situ time series measurements of porewater chemical composition obtained between 10:00 AM July 10, 2004 and 5:00 AM July 11, 2004. The two matching graphs on the top display water level measured at the Fort Pulaski NOAA buoy (dotted line) and the same water level data with a lag of 1:48 hrs to represent the salt marsh tide (solid line).

Mathematical model

The mathematical model was run for a fifteen-day simulation. The last four days of output are shown in Figure 19. Figure 19a. shows the overlying water simulated by the model. Figure 19 b.- f. represents the simulated time series profiles of the four chemical species in the model, with depths of 1, 3, 5, 7, and 9 cm, respectively. Figure 19b shows that oxygen has penetrated the sediment to one centimeter deep. The model is optimized so that iron oxides can develop from completely reduced initial conditions, so the modeled oxygen flux is allowed to go deeper than what we observe in the field. This oxygen profile is easily linked to the tide shown in Figure 19a. During high tide, oxygen is at a minimum concentration (~50 μM). Correspondingly, during low tide oxygen is at its greatest concentration of ~120 μM. The model was built to account for the availability of oxygen from the atmosphere at low tide and the overlying water at high tide.

At 3 cm deep in the sediment, iron oxide has developed over the course of the 15-day run and reached a steady concentration of approximately 100 μM. Iron oxides are made possible in the model by overlap of Fe^{2+} and oxygen, so their constant existence here prove that Fe^{2+} can be pushed up to shallow sediment where oxygen has been drawn down. Again, the mathematical model shows an idealized situation: Fe-oxides exist at one depth only, which is deeper in the sediment, perhaps, than in the real world because oxygen is able to penetrate deeper in the model than in the real world. Also at this depth, during low tide, there is a surplus of oxygen with no Fe^{2+}, as if the oxygen titrated any Fe^{2+} out of the sediment, and during high tide there is excess Fe^{2+}, which was pushed up with the high tide from deeper in the sediment and removed all the oxygen at that depth.

At 5 cm, large amounts of Fe^{2+} dominate the sediment, which are transported up from below with porewater advection in the flood tide. At 7 cm, there are substantial amounts of Fe^{2+} (> 200 μM) and hydrogen sulfide, which has slowly ascended the sediment over the course of fifteen days and is beginning to reach a consistent concentration and depth.

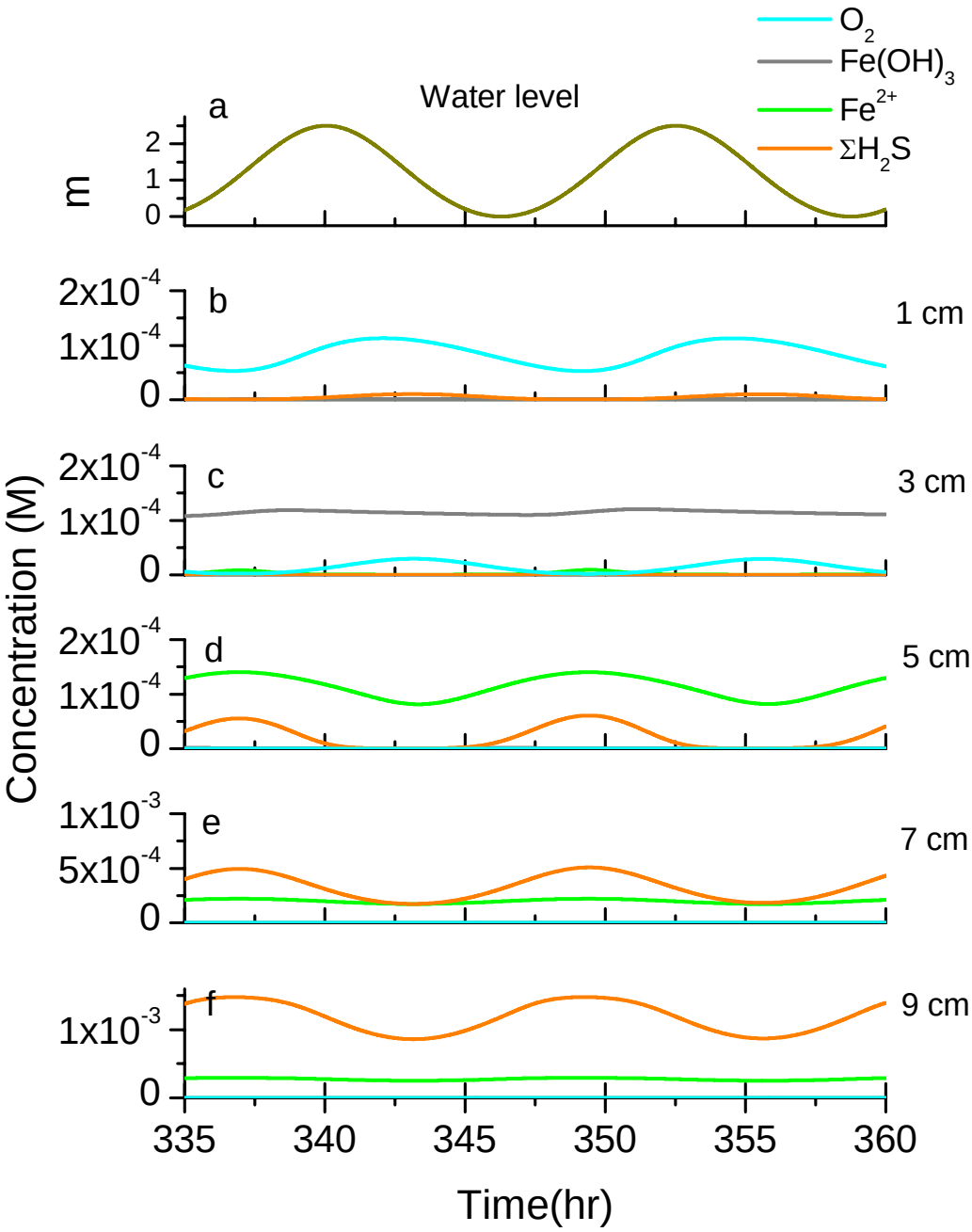

Figure 19. Model output after a fifteen day simulation. The plot represents the last day of the simulation. a: Overlying water level, which is the tides simulated by the model (blue). b-f: Concentration of chemical species in M. Chemical species: $Fe(OH)_3$ (gray), Fe^{2+} (green), O_2 (blue), and ΣH_2S (orange).

Mass balance

The results of the mass balance calculation indicate that the model is indeed mass balanced. Average values for the difference between transport-influenced flux and reaction-influenced flux were always less than $8.7 \times 10^{-9} \frac{moles}{cm^2 \cdot \min}$.

Error Analysis

Multiple simulations were made with a simplified version of the model to test model sensitivity. The numerical solution to the transient transport equation for advection and diffusion (reactions were turned off for these tests) computed by the model was compared to an analytical solution. For each test, Δz and/or Δt were varied and Peclet, Courant, and percent error were observed. Results (Table 4) include Δz, Δt, percent error and the Peclet and Courant numbers associated with each model run. The numerical model contained a few minor differences not accounted for by the analytical solution, most importantly that advection varied as a function of time. However, the tides were represented in the analytical solution because the concentration of the species tested (oxygen) varied with time as a result of the tidally-induced boundary at the top of the model space. Error between the numerical and analytical solutions was calculated using Equation 6:

$$\frac{C_{ANALYTICAL} - C_{NUMERICAL}}{C_{ANALYTICAL}} * 100 \qquad 6.$$

Table 4. Error analysis results for simplified transport model. D is constant: 1.4 x10^{-3} cm^2 min^{-1}. Advection: 5 x10^{-3} cm min^{-1}, Δz and Δt are varied in the model, and Peclet, Courant, and percent error are observed. Parameters used in the full diagenetic model are in bold.

Δt	Δz (cm min^{-1})	Peclet #	Courant #	% error
1.00	0.10	0.36	0.05	3.69
1.00	0.05	0.18	0.10	3.70
1.00	0.03	0.09	0.20	Output unstable
1.00	0.01	0.04	0.50	Output unstable
0.50	0.2	0.71	0.01	3.61
0.50	**0.1**	**0.36**	**0.03**	**3.64**
0.50	0.05	0.18	0.05	3.65
0.50	0.03	0.09	0.10	Output unstable
0.25	0.1	0.36	0.01	2.56
0.25	0.05	0.18	0.03	2.57
0.25	0.03	0.09	0.05	2.57

Results show increasing error and decreasing Peclet numbers as Δz grows smaller with a constant Δt. As Δt shrinks, the error decreases. According to these results, the ideal node spaces in time and distance for the model would be Δt = 0.25, and Δz = 0.1. However, this simplified model does not account for the extensive reaction network and suite of chemical species of the full model, which requires too much processing time to run at these ideal parameters. The usable parameters from the table with the lowest Peclet number and error that gave stable results are in bold. These are the parameters used in the full diagenetic model.

CHAPTER 4

DISCUSSION

The purpose of this research was to characterize tidal effects on the direction and magnitude of porewater advection and to investigate the subsequent changes of the biogeochemistry in the top ten cm of salt marsh tidal creek sediment, where organic matter remineralization is likely to be driven by microbial iron reduction (Lowe et al. 2000).

Core Chemical Profiles

The chemical depth profile from the tidal creek sediment core (Figure 12) showed accumulation of iron oxides near the SWI. Reduced iron and dissolved ferric iron both reached a maximum at the same depth. The implication from this profile is that iron in the system is in the process of being oxidized or reduced. If iron is periodically reoxidized, then it is possible for it to compete as a terminal electron acceptor in the remineralization of organic matter. Additional core profiles from other summers (Figure 13) indicate that this process may be periodic and consistent throughout the years. The core profiles indicate that the saltmarsh sediment geochemistry was not at steady state, and warranted further investigation into the dynamics of the system. We began this investigation by monitoring tidal action in the saltmarsh and observing geochemical species concentrations over tidal cycles.

Well Water Data

Well water data was collected for two reasons. The most important was to determine the direction of tidally-induced porewater advection with respect to the tides.

The other reason was to verify that water level data taken from a NOAA buoy 30 miles away could be used as a proxy for the local tide.

Well data (Figure 15 & Figure 16) calculations show that advection can reach between 15-20 cm hr^{-1}, if not faster, in these fine-grained sediments. However, questions arise about the direction of tidal flow that these measurements do not address. For example, tidally-induced porewater advection probably has a lateral component that needs to be considered. The measurement does distinguish the vertical direction of the tides through the sediment at the sampling site-- the wells with the deepest screens filled first. Therefore, most of the vertical flood tide advection over the first 15-30 cm must be from the sediment depth rather than the SWI in creek bank sediments. In contrast, measurements taken in the mud flat region of the same salt marsh show that water may percolate from the SWI at flood tide (Taillefert et al., 2006).

Neither June nor September monitoring well data indicate any tidal influence at 24 inches (~60 cm) depth in the sediment (Figure 15), suggesting that the depth of tidal intrusion in the sediment may be less than 60 cm. These data suggest that the bulk of the tide comes through laterally at a depth higher than 60 cm. Tidal flow through sediments may occur when incoming tide water pushes against the sediment and creates hydraulic pressure along the banks of adjacent tidal creeks. This pressure forces tide water deeper into creek bank sediments, where it may be pushed laterally to the bottoms of other tidal creeks through high permeability sand layers (Figure 20).

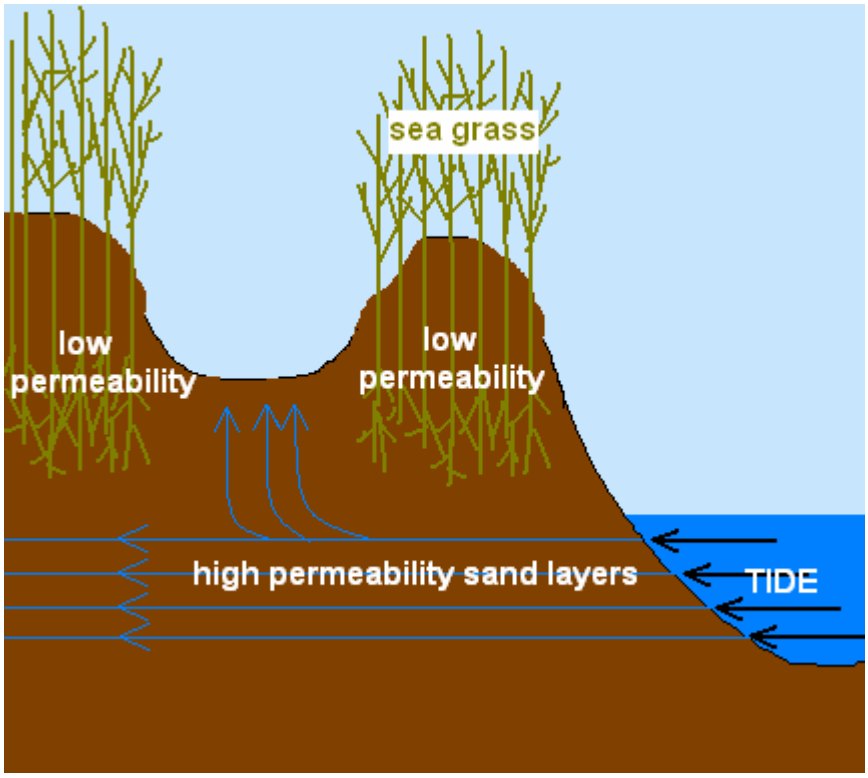

Figure 20. Illustration of creek porewater tidal advection concept. Incoming tide water pushes porewaters through high-permeability sand layers deeper into the creek bank until they eventually surface through the bottom of an adjacent creek bank. In this way, the tide could produce vertical advection in the bottom of an intertidal creek bank sediment.

Voltammetric Time Series Data

In the June, 2003 data set, during the first ebb tide, Fe^{2+} appears at the SWI. It is unclear what the origins of this Fe^{2+} are, but overlying water is suspect because: (1) it contains Fe^{2+} in even greater concentrations than at the SWI, and (2) we suspect the ebb tide draws dissolved oxygen from the overlying water to the sediment. Huettel et al. (1998) showed that when water flows over rippled sediment, some water is forced into the sediment below the ripples and pushes reduced porewater out of the sediment behind the ripples (Figure 21). A similar process may occur in creek banks, except that ripples

are replaced by slip-off slopes that build during meandering of water. Perhaps this mechanism is at work here, causing Fe^{2+} to appear at the SWI during ebb tide.

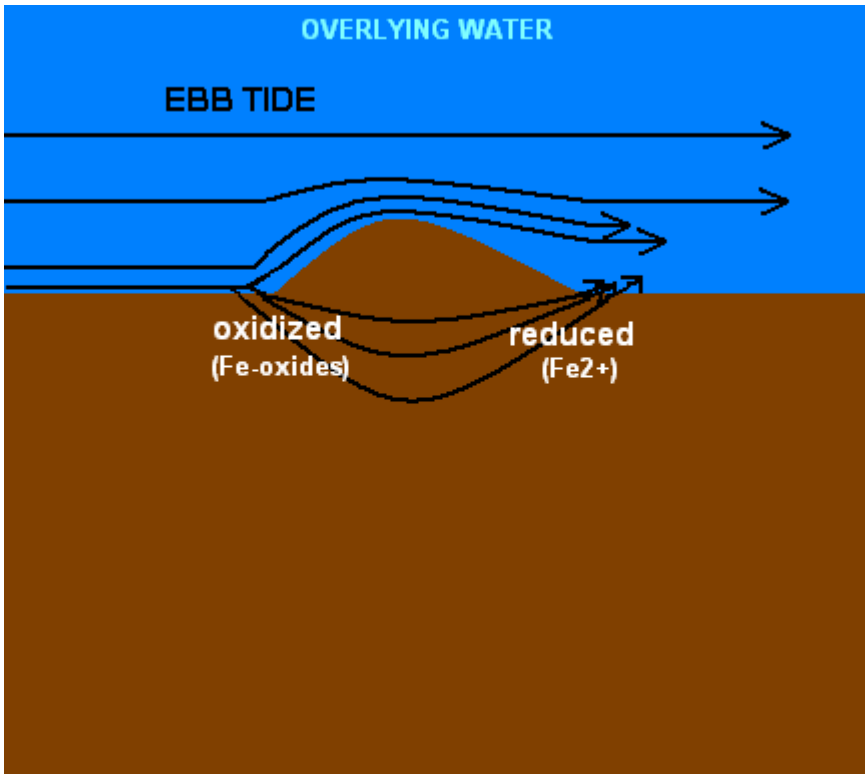

Figure 21. Illustration of possible effect of ebb tide on slip-off slopes in intertidal salt marsh creek, adapted from Huettel et al., (1998).

Fe^{2+} appears to have been absent at the SWI during the first low tide. Presumably, O_2 was available from the atmosphere to oxidize the Fe^{2+} to solid iron oxides— a very rapid chemical process (Stumm and Morgan 1996).

Deeper in the sediment, ΣH_2S concentrations were higher just before and after low tide (no measurements were taken during low tide). Tidal data do not directly indicate the time when tidally-induced porewater movement was stopped or slowed enough so that tidally-induced advection could no longer dominate the sediment. The

rise in ΣH_2S near low tide may be attributable to local or non-local SRB activity. However, the rise in ΣH_2S with the ebb and low tides may be due to lateral advection from other sulfate-reducing zones, or higher in the sediment where $FeS_{(s)}$ was oxidized as the strong tide pushed through the sediment. We observed a very similar trend in the July, 2004 data set (Figure 18) where ΣH_2S concentrations at 7 and 11 cm deep rose at the end of ebb tide and at low tide. Additionally, Figure 18 shows a similar Fe^{2+} trend at the SWI, where Fe^{2+} grew in concentration rather substantially during the ebb tide.

In June, 2003 (Figure 17) the flood tide brought about rapid changes in the sediment geochemistry. Almost as if a switch were pulled, Fe^{2+} and ΣH_2S concentrations dropped dramatically at ~18:00 hr while $FeS_{(aq)}$ is seen in comparatively large amounts at 3.5 cm deep. Most likely, $FeS_{(aq)}$ was formed here when Fe^{2+} and ΣH_2S overlapped. The very large standard deviation of this $FeS_{(aq)}$ peak implies very rapid reactions associated with its formation or its loss via precipitation. $FeS_{(aq)}$ is an indicator of $FeS_{(s)}$ precipitation (Theberge and Luther 1997). Perhaps Fe^{2+} and ΣH_2S that disappeared at ~18:00 hr were sequestered as $FeS_{(s)}$. Tidally-induced advection was so strong that even some $FeS_{(aq)}$ is evident at the SWI during this strong flushing event.

The July, 2004 (Figure 18) data support the idea of upward vertical flushing of porewaters with the flood tide. As in Figure 17 (10.5 cm), in Figure 18e and g (7 and 11 cm, at ~ 25:00 hr) ΣH_2S concentrations decreased during the flood tide. At the same time, just before the concentration of sulfide decreased in Figure 18e. (7 cm), ΣH_2S doubled in concentration, which suggests that ΣH_2S may have been advected up from below. In June, 2003 (Figure 17) organic-Fe(III) appeared for a short period of time as the tide flooded. This may have been a result of Fe-oxides dissolution (Table 1) by ΣH_2S

(advected from below), and reoxidization in the presence of natural ligands (Taillefert et al. 2000). Fe-oxides were most likely present after the recent low tide oxidized the sediment.

In July, 2004 (Figure 18), as the tide ebbed we observed a strong increase in organic-Fe(III) at the SWI, which may be explained by oxidation of Fe^{2+} as O_2 became more available to the sediment. During high tide, lack of advective transport may have allowed FeRB to dominate the geochemistry near the top of the sediment. In this case, Fe-oxides may have been dissolved and reduced by FeRB, creating Fe^{2+}. This source of Fe^{2+} may explain the organic-Fe(III) we observed at the SWI during ebb tide, as Fe^{2+} was recycled back to Fe(III) when oxygen penetrated the sediment from the overlying water. In July, 2004, during low tide we saw a very strong organic-Fe(III) as a result of O_2 penetration from the atmosphere.

In July, 2004 (Figure 18c) substantial concentrations of Fe^{2+} were measured at the SWI during the second flood tide. This may indicate strong FeRB activity in the sediment. $FeS_{(s)}$ that grew concurrently at the SWI was probably formed with some of this excess Fe^{2+} and can explain the whereabouts of ΣH_2S missing from deeper in the sediment. The effects of strong vertical advection on the sediment geochemistry can also be seen at 25:20 hr throughout the data set. At the SWI, Fe^{2+}, ΣH_2S and $FeS_{(aq)}$ grew in concentration, while organic-Fe(III) dropped. ΣH_2S decreased at 7 and 11 cm, and $FeS_{(aq)}$ decreased at 11 cm deep. These very rapid changes suggest that tidal advection pushes sulfide toward the SWI and that chemical or microbial iron reduction may be ongoing near the SWI. Overall, these data indicate that tidal advection may be dominant

during flood tide in this sediment, and thus may dictate the biogeochemistry in intertidal saltmarsh tidal creeks as a whole.

Organic-Fe(III) complexes may also form at depth during ebb tide. Our results indicate that when the tide ebbs, it draws oxidized species back into the sediment. In-situ voltammetric measurements did not include detection of O_2 in July, 2004. In June, 2003, O_2 measurements were made, but O_2 was detected neither in the sediment nor at the SWI, suggesting that oxygen introduced into the sediment rapidly oxidized Fe^{2+} (or other chemical species) and was not present long enough to be detected. Indeed, our in-situ time series data (Figure 18) report oxidized organic-Fe(III) at 7 cm depth, which suggests that the tides may be associated with redox changes in the sediment. In addition, solid phase data indicate accumulation of Fe-oxides in the first few cm of the sediment (Figure 12).

As a result of the strong, semidiurnal, tidally-induced advection measured in the salt marsh, we consider geochemical transport in the sediment to be advection-dominated. The subsequent rapid advection of porewaters at flood and ebb tide in intertidal sediments may move Fe^{2+}, organic-Fe(III), and O_2 quickly enough to rapidly recycle a very important substrate for FeRB in the remineralization of organic matter. Further evidence can be found in the depth profiles of cores that show overlap of reduced and oxidized species (Figure 12). For these species to coexist would require physical transport to be faster than the associated biogeochemical reactions that take place there. As mentioned in Chapter 1, although sulfate reduction is stoichiometrically more efficient than iron reduction because it can oxidize more organic carbon per unit mole of substrate reduced (Table 1), iron reduction is thermodynamically more efficient (at standard

temperature and pressure). In addition, while oxic environments completely inhibit SRB, they only partially inhibit FeRB activity. If iron reduction is only limited by the availability of substrates, and if the tides allow deeper penetration of oxidized species and infusion of reduced iron to the SWI, we may expect significant microbial iron reduction to be possible in this type of environment. FeRB domination has been detected in the field previously: Oxygen diffuses across the roots of *S. alterniflora* and then oxidizes Fe^{2+} in the sediment in the root vicinity (Sundby et al. 1998, Holmer et al. 2002). Gribsholt et al. (2003) report that in the vicinity of *S. alterniflora* rhizospheres and in the sediment adjacent to crab burrows, microbial Fe(III) reduction dominates over sulfate reduction in the oxidation of organic matter. Fiddler crab burrows may increase the sediment surface area in salt marshes by up to 60% (Katz 1980), which would allow more oxidation of the sediment. Kostka et al. (2003) found that burrowing causes the sediments within 4 cm of burrow walls to be dominated by Fe(III) reduction over sulfate reduction, with Fe(III) reduction responsible for 54-86% of total carbon oxidation. Active FeRB have been found near aquatic macrophytes (King and Garey 1999, Lowe et al. 2000, Kostka et al. 2002a). Our results suggest that tidally-induced penetration of oxygen (or oxidized species) is responsible for oxidizing the sediment, thus inhibiting the potential for SRB activity in the degradation of organic matter.

SRB activity has been reported to increase with temperature (Howarth and Giblin 1983, Koretsky et al. 2003). In June, 2003, SRB may have dominated (at depth), generating very high concentrations of ΣH_2S (~1300 μM). In contrast, very low concentrations of ΣH_2S at depth in the July, 2004 data set indicate that SRB activity was not strong there at that time. The temperature of the July, 2004 sediment was lower than

that of the June, 2003 sediment, and the relative shortage of sulfide indicates that FeRB activity may be more dominant than SRB in these sediments (near the SWI). This is evidenced by substantially higher concentrations of Fe^{2+} near the SWI in July, 2004 than in June, 2003.

Mathematical Model

The purpose of the mathematical model (Figure 19) was to test the hypothesis that tides affect redox geochemical profiles. Specifically, we wanted to test our hypothesis that porewater Fe^{2+} is pushed towards the SWI at flood tide and oxidized below the SWI by O_2 at ebb tide to recycle iron oxide and make it available for NOM oxidation. Over all time in the model (Figure 19), some oxygen diffuses into the sediment from the overlying water, as seen in Figure 19b. As it penetrates deeper into the sediment, it oxidizes Fe^{2+} and eventually is used up completely (Figure 19c in the case of low tide and Figure 19d in the case of high tide). While these occurrences are much deeper than saltmarsh measurements indicate (O_2 in this sediment typically doesn't reach below a few mm), they are meant to act as a diagnostic tool for mechanisms at work in this type of muddy, redox-sensitive sediment.

ΣH_2S and Fe^{2+} vary with a periodicity that matches the tides. During flood tide, concentrations of Fe^{2+} and ΣH_2S are higher in shallower sediment, and during ebb tide they have lower concentrations throughout the simulated sediment. ΣH_2S is found deeper in the sediment than Fe^{2+}, which reflects what we have measured in the field (Figure 17, Figure 18, and other data (Taillefert et al. 2006)) and what is considered standard redox zonation of sediment (Froelich et al. 1979). ΣH_2S slowly rose through the sediment over the last four days of simulation, but appears to have leveled off with a constant concentration oscillation that matches the tides. FeS created by the overlap of Fe^{2+} and ΣH_2S is not shown.

At 3 cm, Fe-oxides slowly grew in concentration over both high and low tides until they eventually leveled off with a very slight tidal oscillation in concentration.

Therefore, it is evident that the species simulated by the model are approaching steady state.

Overall, the simulated chemical species display obvious tidally-induced concentration maxima. Diffusion and bioturbation parameters in the model do match real published values (Table 3), but advection in the model is grossly underrepresented with respect to real measured advection values. Nevertheless, the model output does indicate a system strongly dominated by tidal advection that can connect reduced species (Fe^{2+}) with oxidized (O_2).

Currently, the model does not include all of the processes suspected of being at work in the salt marsh. It includes a term that represents $FeS_{(s)}$ precipitation, but does not include $FeS_{(s)}$ as a separate species. $FeS_{(s)}$ is represented in the model only as a sink of sulfide and iron. Future electrochemical measurements and refinement of electrochemical measurement techniques will hopefully provide more insights into the cycling of these species. Additional features that would benefit the model are three-dimensional bioirrigation due to crab burrows, oxygen penetration through macrophyte roots, and incorporation of other redox species such as NO_3^-, NH_4^+, MnO_2, and Mn^{2+}.

Bioturbation

The diagenetic modeling community generally differentiates between types of animal activity in the sediment. Bioturbation usually refers to sediment mixing as a result of animal digging, and typically plays a role near the SWI. Bioirrigation refers to ventilation of animal burrows with O_2-rich water, and how this affects sediment geochemistry (Boudreau 1997). Bioirrigation may have an influence deep in the sediment.

The effects of burrows are not actively considered in this model. However, because the diagenetic modeling community considers bioirrigation the dominant physical transport mechanism in coastal marine sediments, its influence on transport compared to that of advection was evaluated. To do this, the model was stripped down to one species, the reactions removed, and a bioirrigation component added. The bioirrigation term was taken from the 1-dimensional adaptation of Aller's (1980) Tube Model taken from Boudreau, (1997):

$$bioirrigation = \alpha(z)(\overline{C} - C_o) \qquad 7.$$

where z is depth (cm), $\overline{C}$ the mean species concentration at depth z, and C_o the species chemical concentration at the sediment-water interface. α is a term to represent the non-local exchange rate at depth z (Equation 8),

$$\alpha(z) = \frac{2Dr_1}{(r_2^{\,2} - r_1^{\,2})(\bar{r} - r_1)} \qquad 8.$$

where $\bar{r}$ is the radial distance at which the concentration equals the mean value $\overline{C}$, r_2 is the distance from the midpoint of the burrow to the furthest point in the sediment subject to irrigation, and r_1 is the radius of the burrow. $\alpha(z)$, taken from Emerson et al. (1984), was 6.3 yr^{-1}.

The calculated difference between output from the transient advective transport models containing bioirrigation and without bioirrigation (both normalized to Co) was between 0.07 and 1.29 %. These results indicate that the effects of bioirrigation on chemical species transport may not be important when compared to the effects from tidally-induced advection in intertidal salt marsh creek bank sediment. Due to skepticism of this 1-D method (i.e., Furukawa et al. 2001) and much research conducted on

bioirrigation (Aller 1982, Kristensen 1988, Aller and Aller 1998, Furukawa et al. 2001), it is evident that further study on the effects of bioirrigation in this environment would be useful

The data presented in this paper suggest that advection, dominated by the tides, may cause rapid recycling of iron. Reduced iron in anoxic porewaters at depth may ascend toward the oxic SWI, and oxidized iron (or oxygen) may descend from oxic toward anoxic sediments. Availability of oxidized iron would promote the growth and activity of FeRB. Increased iron reduction by FeRB would result in increased carbon remineralization rates in shallow saltmarsh sediments, where organic matter input and primary production are extremely high. If this is the case, respiration may be more important in intertidal salt marsh creek banks than previously thought. If tidal advection drives respiration strongly enough in intertidal salt marsh creek banks, and perhaps other salt marsh environments (i.e., rippled sediment) it may be that respiration wields local dominance over photosynthesis, and these sediments are an overall sink for organic carbon, and a source for inorganic carbon. Recent evidence suggests that continental margins may be important areas for carbon sedimentation (Liu et al. 2000), and that extensive remineralization must take place in these coastal areas to account for the disparity between land-derived carbon delivered to the seas from rivers and the amount of land-derived carbon found in marine sediment (Hedges 1997).

CHAPTER 5

CONCLUSIONS

In this study, sediment core profiles, well water level measurements, voltammetry, and mathematical modeling were used to investigate the role of tidal forcing on the cycling of iron in intertidal saltmarsh sediments. This study introduces the first in-situ voltammetric porewater time series data taken in intertidal salt marsh sediments over several tidal cycles. Voltammetry data demonstrate porewater advection with the tides, showing a tidal influence on the depths and concentrations of redox species iron and sulfide. In addition, well water data obtained in the salt marsh confirm that strong porewater advection occurs within the sediment with a rapid vertical flow component. Tidal and voltammetric data seem to correlate. During flood tide, reduced species such as sulfide are pushed toward oxidized sediment, and during ebb tide, the oxic zone grows deeper as reduced species are oxidized in the sediment. This indicates an oxic-anoxic oscillation of the sediment at certain depths. Tidal advection may drive FeRB activity by replenishing oxidized iron, resulting in an increased rate of carbon remineralization in salt marsh sediments. As a result, respiration may be stronger in salt marsh sediments than is commonly thought. Mathematical model results suggest that it may be possible to simulate this dynamic environment using tidally-induced transport parameters and known biological and chemical reactions.

REFERENCES

Abrams J. W., and D.B. Nedwell. (1978) Inhibition of methanogenesis by sulfate reducing bacteria competing for transferred hydrogen. *Arch. Microbiol.* **117**, 89-92.

Aller, R.C. (1980) Quantifying solute distribution in the bioturbated zones of marine sediments by defining an average microenvironment. *Geochimica et Cosmochimica Acta* **44**, 1955-1965.

Aller, R.C., and J.Y Aller. (1998) The effect of biogenic irrigation intensity and solute exchange on diagenetic reaction rates in marine sediments. *J. Mar. Res*. **56**, 905-936.

Alongi D. M. (1998) *Coastal Ecosystem Processes*. CRC Press.

Berner R. A. (1980) *Early Diagenesis: A Theoretical Approach*. Princeton University Press.

Boetius A., K. Ravenschlag, C.J. Schubert, D. Rickert, F. Widdel, A. Gleseke, R. Amann, B.B. Jorgensen, U. Witte, and O. Pfannkuche. (2000) A marine microbial consortium apparently mediating anaerobic oxidation of methane. *Nature* **407**, 623-626.

Bolster, C.H., and J.E. Saiers (2002) Development and evaluation of a mathematical model for surface-water flow within the Shark River Slough of the Florida Everglades. *Journal of Hydrology* **259** 221-235.

Boudreau B. B. (1997) Diagenetic Models and their Implementation, Springer.

Brendel P. J., and G.W. Luther III. (1995) Development of a Gold Amalgam Voltammetric Electrode for the Determination of Dissolved Fe, Mn, O2, S(-II) in Porewaters of Marine and Freshwater Sediments. *Environ. Sci. Technol.* **29**, 751-761.

Bull D. C., and M. Taillefert. (2001) Seasonal and topographic variations in porewaters of a southeastern USA salt marsh as revealed by voltammetric profiling. *Geochemical Transactions (online computer file).*

Canfield D. E., Jorgensen, B.B., Fossing, H., Glud, R., Gundersen, J., Ramsing, N.B., Thamdrup, B., Hansen, J.W., Nielsen, L.P., Hall, P.O.J. (1993) Pathways of

organic carbon oxidation in three continental margin sediments. *Marine Geology* **113**, 27-40.

Canfield D. E., Thamdrup, B., Hansen, J.W. (1993) The anaerobic degradation of organic matter in Danish coastal sediments: Iron reduction, manganese reduction, and sulfate reduction. *Geochimica et Cosmochimica Acta* **57**, 3867-3883.

Doong R., and B. Schink. (2002) Cysteine-Mediated Reductive dissolution of poorly crystalline Iron(III) oxides by Geobacter sulfurreducens. *Environ. Sci. Technol.* **36**, 2939-2945.

Emerson, S., R. Jahnke, and D. Heggie. (1984) Sediment-water exchange in shallow water estuarine sediments. Jour. Mar. Res. v. 42, 709-730

Fabritz J. E. (1995) A two dimensional numerical model for simulating the movement and biodegradation of contaminants in a saturated aquifer, University of Washington.

Fogel M. L., E. K. Sprague, A.P. Gize, and R. W. Frey. (1989) Diagenesis of Organic Matter in Georgia Salt Marshes. *Estuarine, Coastal and Shelf Science* **28**, 211-230.

Froelich, P.N., G.P. Klinkhammer, M.L. Bender, N.A. Luedtke, G.R. Heath, D. Cullen, P. Dauphin, D. Hammond, B. Hartman, and V. Maynard. (1979) Early oxidation of organic matter in pelagic sediments of the eastern equatorial Atlantic: suboxic diagenesis. *Geochimica et Cosmochimica Acta* **43**, 1075-1090.

Furukawa, Y., R.A. Socki, L. Elrod, and K.K. Bissada. (2001) Two-dimensional numerical modeling of geochemical interactions between infauna and sediments during early diagenesis of burrowed shelf carbonate sediments in the Dry Tortugas, Florida. *Geochimica et Cosmochimica Acta*

Gaillard J. F., and C. Rabouille. (1992) *Using Monod kinetics in geochemical models of organic carbon mineralization in deep-sea surficial sediments. In: Deep-Sea Food Chains and the Global Carbon Cycle*. Kluwer Academice Publishers.

Glud, R.N., J.K. Gundersen, B.B. Jorgensen, N.P. Revsbech, and H.D. Schulz. (1994) Diffusive and total oxygen uptake of deep-sea sediments in the eastern South Atlantic Ocean: in situ and laboratory measurements. *Deep-Sea Research I* **41** 1767-1788.

Grasshoff K., K. Kremling, and M. Ehrhardt. (1999) *Methods of Seawater Analysis*. Wiley-VCH.

Gribsholt B., J. E. Kostka, E. Kristensen. (2003) Impact of fiddler crabs and plant roots on sediment biogeochemistry in a Georgia saltmarsh. *Marine Ecology Progress*

Series **259**, 237-251.

Hall P. O. J., and R.C. Aller. (1992) Rapid, small-volume, flow injection analysis for SCO2 and NH4+ in marine and freshwaters. *Limnol. Oceanogr.* **37**, 1113-1119.

Hedges J. I., R.G. Keil, R. Benner. (1997) What happens to terrestrial organic matter in the ocean? *Organic Geochemistry* **27**, 195-212.

Hines M. E., S.L. Knollmeyer, and J.B. Tugel. (1989) Sulfate reduction and other sedimentary biogeochemistry in a northern New England salt marsh. *Limnol. Oceanogr.* **34**, 578-590.

Holmer M., B. Gribsholt, E. Kristensen. (2002) Effects of sea level rise on growth of Spartina anglica and oxygen dynamics in rhizosphere and saltmarsh sediments. *Marine Ecology Progress Series* **225**, 197-204.

Howarth, R. W., and A. Giblin. (1983) Sulfate reduction in the salt marshes at Sapelo Island, Georgia. *Limnology and Oceanography* **28**: 70-82

Howes B. L., R.W. Howarth, J.M. Teal, I. Valiela. (1981) Oxidation-reduction potentials in a salt marsh: Spatial patterns and interactions with primary production. *Limnol. Oceanogr.* **26**(2), 350-360.

Huettel, M., W. Ziebis, S. Forster, and G.W. Luther, III. (1998) Advective transport affecting metal and nutrient distributions and interfacial fluxes in permeable sediments. *Geochimica et Cosmochimica Acta* **62** 613-631.

Hughes, C.E., P. Binning, and G.R. Willgoose. (1998) Characterisation of the hydrology of an estuarine wetland. *Journal of Hydrology* **211** 34-49.

Joye S., and J.T. Hollibaugh. (1995) Influence of sulfide inhibition of nitrification on nitrogen regeneration in sediments. *Science* **270**, 623-625.

Kappler A., and D.K. Newman. (2003) Formation of Fe(III)-minerals by Fe(II)-oxidizing photoautotrophic bacteria. *Geochimica et Cosmochimica Acta* **68**(6), 1217-1226.

King G. M. (1988) Patterns of sulfate reduction and the sulfur cycle in a South Carolina salt marsh. *Limnol. Oceanogr.* **33**, 376-390.

Koretsky C. M., C.M. Moore, K.L. Lowe, C. Meile, T. DiChristina, P. Van Cappellen. (2003) Seasonal oscillation of microbial iron and sulfate reduction in saltmarsh sediments (Sapelo Island, GA, USA). *Biogeochemistry* **64**, 179-203.

Kostka J. E., and G.W. Luther III. (1994) Partitioning and speciation of solid phase iron in saltmarsh sediments. *Geochimica et Cosmochimica Acta* **58**, 1701-1710.

Kostka J. E., A. Roychoudhury, and P. Van Cappellen. (2002) Rates and controls of anaerobic microbial respiration across spatial and temporal gradients in saltmarsh sediments. *Biogeochemistry* **60**, 49-76.

Kostka J. E., B. Gribsholt, E. Petrie, D. Dalton, H. Skelton, E. Kristensen. (2002a) The rates and pathways of carbon oxidation in bioturbated saltmarsh sediments. *Limnol. Oceanogr.* **47**(1), 230-240.

Kristensen, E. (1988) *Benthic fauna and biogeochemical processes in marine sediments: microbial activities and fluxes, in Nitrogen Cycling in Coastal Marine Environments*, T.H. Blackburn and J. Sorensen, eds., John Wiley & Sons Ltd, Chichester, 275-299.

Liu K.-K., L. Atkinson, C.T.A. Chen, S. Gao, J. Hall, R.W. Macdonald, L. Talaue McManus and R. Quinones. (2000) Exploring Continental Margin Carbon Fluxes on a Global Scale. *E.O.S.* **81**(52).

Lowe K. L., and T.J. DiChristina. (2000) Microbial and geochemical characterization of microbial Fe(III) reduction in salt marsh sediments. *Geomicrobiology Journal* **17**, 163-178.

Mann, C.J., and R.G. Wetzel. (2000) Hydrology of an impounded lotic wetland-subsurface hydrology. *Wetlands* **20** 33-47.

Montague C. L. (1982) The influence of fiddler crab burrows and burrowing on metabolic processes in saltmarsh sediment. In *Estuarine Comparisons* (ed. V. S. Kennedy). Academic Press.

Mwamba, M.J., and R. Torres. (2002) Rainfall effects on marsh sediment redistribution, North Inlet, South Carolina, USA. *Marine Geology* **189** 267-287.

Reimers, C.E., K.M. Fischer, R. Merewether, K.L. Smith Jr., and R.A. Jahnke. (1986) Oxygen microprofiles measured in situ in deep ocean sediments. *Nature* **320** 741-744

Reimers, C., H.A. Stecher III, G.L. Taghon, C.M. Fuller, M. Huettel, A. Rusch, N. Ryckelynck, and C. Wild (2004) In situ measurements of advective solute transport in permeable shelf sands. *Continental Shelf Research* **24** 183-201.

Rickard, D. (1995) Kinetics of FeS precipitation: Part 1. Competing reaction mechanisms. *Geochimica et Cosmochimica Acta* **59** 4367-4379.

Rickard D., and G. W. Luther III. (1997) Kinetics of pyrite formation by the H2S oxidation of iron(II) monosulfide in aqueous solutions between 25 and 125oC: the mechanism. *Geochimica et Cosmochimica Acta* **61**, 135-147.

Roden E. E., D. Sobolev, B. Glazer, and G.W. Luther III. (2004) Potential for Microscale Bacterial Fe Redox Cycling at the Aerobic-Anaerobic Interface. *Geomicrobiology Journal* **21**, 379-391.

Rozan T. F., M. Taillefert, R.E. Trouwborst, B. T. Glazer, S. Ma, J. Herszage, L.M. Valdes, K.S. Price, G. W. Luther III. (2002) Iron-sulfur-phosphorus cycling in the sediments of a shallow coastal bay: Implications for sediment nuitrient release and benthic macroalgal blooms. *Limnol. Oceanogr.* **47**(5), 1346-1354.

Schultz, G., and C. Ruppel. (2002) Constraints on hydraulic parameters and implications for groundwater flux across the upland-estuary interface. *Journal of Hydrology* **260** 255-269.

Steefel C. I., and K.T.B. MacQuarrie. (1996) Approaches to Modeling of Reactive Transport in Porous Media. *Reviews in Mineralogy* **34**, 83-129.

Stookey L. L. (1970) Ferrozine: a new spectrophotometric reagent for iron. *Analytical Chemistry* **42**, 779-781.

Strang G. (1968) On the construction and comparison of difference schemes. *SIAM J Numer Anal* **5**, 506-517.

Stumm W., and J.J. Morgan. (1996) *Aquatic Chemistry*. John Wiley and Sons, Inc.

Sundby B., C. Vale, I. Cacador, F.M. Catarino, M.J. Madureira, F. Caetarino. (1998) Metal-rich concentrations on the roots of saltmarsh plants: mechanism and rate of formation. *Limnol. Oceanogr.* **43**, 245-252.

Taillefert M., A.B. Bono, and G.W. Luther III. (2000) Reactivity of freshly formed Fe(III) in synthetic solutions and (Pore)waters: Voltammetric evidence of an aging process. *Environ. Sci. Technol.* **34**, 2169-2177.

Taillefert M., and T.F Rozan. (2002) Environmental Electrochemistry Analyses of Trace Element Biogeochemistry. In *ACS SYmposium Series 811*. American Chemicsl Society.

Taillefert, M., S. Neuhuber, and G. Bristow (2006). The effect of tidal forcing on iron cycling in intertidal salt marsh sediments. *Marine Chemistry*. SUBMITTED.

Theberge, S. M., G. W. Luther, III and A. M. Farrenkopf. (1997). On the existence of free and metal complexed sulfide in the Arabian Sea and its OMZ. *Deep Sea Res.* **44**, 1381-1390.

Thamdrup B., H. Fossing, and B. B. Jorgensen. (1994) Manganese, iron and sulfur cycling in a coastal marine sediment, Aarhus Bay, Denmark. *Geochimica et Cosmochimica Acta* **58**(23), 5115-5129.

Trouwborst R. E. (1999) Measurement of redox species in estuarine sediments using voltammetric microelectrodes. *Not published*.

Valentine D. L., and W. S. Reeburgh. (2000) New perspectives on anaerobic methane oxidation. *Environmental Microbiology* **2**, 1-9.

Yao W., and F.J. Millero. (1996) Oxidation of hydrogen sulfide by hydrous Fe(III) oxides in seawater. *Mar. Chem.* **52**, 1-16.

Zinder B., G. Furrer, and W. Stumm. (1986) The coordination chemistry of weatherig: II. Dissoolution of Fe(III)-oxides. *Geochimica et Cosmochimica Acta* **50**, 1861-1869.

Zysset A., and F. Stauffer. (1992) Modeling of microbial processes in groundwater infiltration systems. In *Mathematical Modeling in Water Resources* (ed. T. F. Russell, R.E. Ewing, C.A. Brebbia, W.G. Gray and G.F.Pinder). Computational Mechanics Publications.